Applied Radiation and Isotopes 226 (2025) 112219

Contents lists available at ScienceDirect

Applied Radiation and Isotopes

journal homepage: www.elsevier.com/locate/apradiso

Luminescence enhancement and thermal stability of alkali co-doped Eu^{3+}: $LaMgB_5O_{10}$ phosphors

V. Onar [a], E. Ekdal Karali [b], Abeer S. Altowyan [c,**], H. Aydin [d,e], U.H. Kaynar [f], C. Gök [f], M.B. Coban [g], Jabir Hakami [h], Y. Ozcan [i], A. Canimoglu [j], N. Can [h,k,*]

[a] Mechanical Engineering Department, Faculty of Technology, Pamukkale University, Kinikli, Denizli, Turkiye
[b] Ege University, Institute of Nuclear Sciences, 35100, Izmir, Turkiye
[c] Department of Physics, College of Science, Princess Nourah bint Abdulrahman University, P.O. Box 84428, Riyadh, 11671, Saudi Arabia
[d] Graphene Application&Research Center, Izmir Katip Celebi University, Izmir, Turkiye
[e] Central Research Laboratories, Izmir Katip Celebi University, Izmir, Turkiye
[f] Bakırcay University, Faculty of Engineering and Architecture, Department of Fundamental Sciences, Menemen, Izmir, Turkiye
[g] Balikesir University, Faculty of Arts and Sciences, Department of Physics, Balikesir, Turkiye
[h] Jazan University, College of Science, Department of Physical Sciences, Physics Division, P.O. Box 114, 45142, Jazan, Saudi Arabia
[i] Department of Biomedical Engineering, Faculty of Technology, Pamukkale University, 20070, Denizli, Turkiye
[j] Nigde Omer Halisdemir University, Faculty of Science, Physics Department, Nigde, Turkiye
[k] Nanotechnology Research Unit, College of Science, Jazan University, P.O. Box. 114, Jazan, 45142, Saudi Arabia

ARTICLE INFO

Keywords:
$LaMgB_5O_{10}$
Eu^{3+}
Alkali co-doping
Photoluminescence
Anti-thermal quenching (ATQ)
Far-red emission

ABSTRACT

Eu^{3+}-activated $LaMgB_5O_{10}$ (LMBO:Eu^{3+}) phosphors were synthesized and systematically investigated to elucidate the role of alkali co-doping (Li^+, K^+) on their structural and luminescence properties. XRD, Raman, and FTIR analyses confirmed the phase purity and revealed subtle lattice distortions upon alkali incorporation, while SEM/EDS verified homogeneous dopant distribution. Photoluminescence spectra are dominated by the characteristic $^5D_0 \rightarrow {}^7FJ$ transitions of Eu^{3+}, with alkali ions inducing pronounced modifications in band distribution and emission intensity. Li^+ co-doping yields a moderate enhancement and redistributes oscillator strength toward the $^5D_0 \rightarrow {}^7F_4$ transition, whereas K^+ co-doping produces nearly an order of magnitude increase in far-red emission. Judd–Ofelt analysis provided intensity parameters (Ω_2, Ω_4, Ω_6), radiative lifetimes, and quantum efficiencies, highlighting the impact of alkali-induced site symmetry perturbations. Temperature-dependent PL measurements revealed distinct quenching and anti-thermal quenching (ATQ) behaviors: undoped Eu^{3+} exhibited conventional quenching with an activation energy of 0.404 eV, K^+ co-doping reduced the barrier to 0.205 eV and triggered moderate ATQ above 470 K, while Li^+ co-doping produced strong ATQ with emission intensity increasing nearly fourfold at 550 K. These findings demonstrate that alkali co-doping not only enhances far-red emission at room temperature but also stabilizes or even amplifies luminescence at elevated temperatures, making LMBO:Eu^{3+},M^+ phosphors promising candidates for high-power pc-WLEDs and plant-growth lighting.

1. Introduction

Rare-earth activated phosphors have long been studied as efficient luminescent materials because of their sharp f–f transitions, high color purity, and long lifetimes, making them suitable for applications in solid-state lighting, lasers, and display technologies (Blasse and Grabmaier, 1994; Jüstel et al., 1998). In addition to their well-established roles in solid-state lighting and display technologies, borate-based phosphors have been investigated for advanced applications — including plasma display panels, high-intensity discharge lamps, optically pumped solid-state lasers, radiation detection, and scintillation systems — further underscoring their versatile technological importance (Jambhale et al., 2025; Tawalare, 2022). In particular, RBO_3, $RAl_3(BO_3)_4$, and $RMgB_5O_{10}$ (R = Y, La–Lu) compounds have emerged as promising candidates for UV-excited high-power emitters in the visible region. Within this context, white LED illumination represents one of the

* Corresponding author. Jazan University, College of Science, Department of Physical Sciences, Physics Division, P.O. Box 114, 45142, Jazan, Saudi Arabia.
** Corresponding author. Department of Physics, College of Science, Princess Nourah bint Abdulrahman University, P.O. Box 84428, Riyadh, 11671, Saudi Arabia.
E-mail addresses: asaltowyan@pnu.edu.sa (A.S. Altowyan), ncan@jazanu.edu.sa (N. Can).

https://doi.org/10.1016/j.apradiso.2025.112219
Received 6 September 2025; Received in revised form 26 September 2025; Accepted 29 September 2025
Available online 30 September 2025

most significant application fields, typically realized via three approaches: a blue semiconductor chip combined with a yellow phosphor; a blue, green, and red tri-emitter combination; or a UV semiconductor source coupled with blue, green, and red phosphors (Dubey et al., 2014; Hölsä and Leskelä, 1985; Lokeswara Reddy et al., 2013; Mitina et al., 2023). Among the wide range of host lattices, borate-based compounds are particularly attractive due to their large band gaps, high chemical and thermal stability, low preparation temperature, and structural diversity that enables the accommodation of various activator ions (Tawalare, 2022; Tiwari and Dhoble, 2025). The coexistence of BO_3 and BO_4 units in borates provides flexible frameworks that suppress non-radiative processes and facilitate efficient luminescence (El Jouhari et al., 1996).

Within this family, lanthanide magnesium pentaborates with the general formula $LnMgB_5O_{10}$ (Ln = La, Gd, Y, etc.) have drawn considerable attention. $LaMgB_5O_{10}$ (LMBO), first synthesized and structurally described by Saubat et al. (1981) and Fouassier et al. (1981), crystallizes in the monoclinic space group $P2_1/c$. Its structure consists of $[B_5O_{10}]^{5-}$ layers linked by La^{3+} and Mg^{2+} cations, forming one-dimensional chains of lanthanide ions well separated by polyborate groups. This topology reduces cross-relaxation and concentration quenching, making LMBO an excellent candidate for rare-earth doping (Sakirzanovas et al., 2011; Volkova et al., 2023). Early investigations already explored its luminescence when doped with Eu^{3+} and Tb^{3+} (Hölsä and Leskelä, 1985; Saubat et al., 1981), establishing the foundation for later optical studies.

Over the past decades, LMBO has been explored with different rare-earth activators, yielding a wide range of emission colors. Dy^{3+} doping produces strong blue (~482 nm, $^4F_{9/2} \rightarrow {}^6H_{15/2}$) and yellow (~578 nm, $^4F_{9/2} \rightarrow {}^6H_{13/2}$) emissions, enabling single-phase white-light generation (Hakami et al., 2025). Sm^{3+} incorporation gives rise to intense orange-red emission bands ($^4G_{5/2} \rightarrow {}^6H_J$), accompanied by well-resolved Stark splitting that reflects strong crystal-field interactions (Sakirzanovas et al., 2011). Tb^{3+}-activated LMBO exhibits efficient green emission ($^5D_4 \rightarrow {}^7F_5$, ~543 nm) with external quantum efficiencies exceeding 75 %, making it competitive with commercial lamp phosphors (Mitina et al., 2023; Tawalare, 2022). More recently, Tm^{3+} doping was reported to yield intense blue emission ($^1D_2 \rightarrow {}^3F_4$), extending the emission palette of LMBO to the short-wavelength region (Volkova et al., 2023). Furthermore, co-doped systems such as Ce^{3+}–Tb^{3+}–Mn^{2+} in LMBO have demonstrated efficient energy transfer and even white-light generation under UV excitation, both in crystalline and glassy phases (El Jouhari et al., 1996). Beyond bulk and glass samples, thin film forms of LMBO and related phases have also been realized; for example, Ce^{3+}/Tb^{3+} co-doped $(La,Gd)MgB_5O_{10}$ nanocrystalline thin films prepared by sol-gel methods exhibit efficient energy transfer and green emission (Lin et al., 2006).

Despite these advances, investigations of Eu^{3+} in LMBO remain relatively limited. Eu^{3+} is one of the most important activators in phosphor research due to its sharp red emission lines ($^5D_0 \rightarrow {}^7F_2$, ~612 nm) with high color purity. Beyond its technological importance for warm white light-emitting diodes (WLEDs), Eu^{3+} is also a valuable spectroscopic probe: the relative intensity ratio of the $^5D_0 \rightarrow {}^7F_2$ and $^5D_0 \rightarrow {}^7F_1$ transitions is highly sensitive to site symmetry and crystal-field strength (Judd, 1962; Ofelt, 1962). Although early optical studies provided valuable insight into Eu^{3+} site symmetry in LMBO (Hölsä and Leskelä, 1985), these pioneering works were limited in scope. In contrast, modern investigations have remained comparatively scarce, especially regarding advanced analyses such as Judd–Ofelt modelling and low-temperature spectroscopy. Such limitations underline the need for renewed investigation, since Eu^{3+} is uniquely suitable for probing host–dopant interactions in LMBO (Mitina et al., 2023; Tawalare, 2022). Moreover, the structural characteristics of LMBO suppress concentration quenching even at elevated dopant concentrations, suggesting that Eu^{3+}-doped LMBO could combine high emission intensity with stable chromaticity (Sakirzanovas et al., 2011; Saubat et al., 1981).

In our previous work, Dy^{3+}-doped LMBO was systematically investigated through X-ray diffraction (XRD), Fourier-transform infrared spectroscopy (FTIR), Raman scattering, scanning electron microscopy (SEM), photoluminescence (PL), CIE chromaticity analysis, and thermal quenching behavior (Hakami et al., 2025). Building on this foundation, the present study extends the investigation to Eu^{3+} doping in LMBO. In addition to applying the same characterization methods, Judd–Ofelt (J–O) analysis, high-temperature PL measurements, and luminescence lifetime studies are performed to provide a deeper understanding of the radiative properties and site environments of Eu^{3+} ions. Through this comprehensive approach, we aim to evaluate $LaMgB_5O_{10}:Eu^{3+}$ as an efficient red-emitting phosphor while also establishing it as a model system for probing structure–property relationships in borate-based hosts, thereby contributing both to fundamental understanding and to the development of next-generation phosphor materials.

2. Materials and methods

2.1. Synthesis

$LaMgB_5O_{10}:Eu^{3+}$ phosphors were synthesized via a microwave-assisted sol–gel combustion method, following a protocol adapted from our previous work on Dy^{3+}-doped LMBO (Hakami et al., 2025). High-purity La_2O_3 (99.99 %), $Mg(NO_3)_2{\cdot}9H_2O$ (≥99.0 %), and H_3BO_3 were used as host precursors, while $Eu(NO_3)_3$ (99.9 %) served as the dopant source. The nitrates were dissolved in dilute nitric acid to obtain homogeneous solutions, which were subsequently mixed and stirred until complete dissolution. Stoichiometric amounts of Eu^{3+} were introduced to achieve doping concentrations of 0.5–7 wt%. After gel formation through gradual heating, the precursor was subjected to microwave irradiation, promoting combustion and initiating crystallization. The resulting powders were annealed at 960 °C for 72 h to enhance crystallinity and ensure uniform dopant incorporation. Compared to conventional solid-state synthesis, the microwave-assisted sol–gel route offers reduced processing time, improved homogeneity, and lower energy consumption.

2.2. Characterization

Structural and morphological properties were examined by X-ray diffraction (XRD, Panalytical Empyrean, Cu Kα radiation, 10–80° 2θ range) with Rietveld refinement, Fourier-transform infrared spectroscopy (FTIR, Thermo Scientific Nicolet iS50), and Raman scattering (Renishaw inVia, 532 nm excitation). Surface morphology and particle distribution were studied using scanning electron microscopy (SEM, JEOL JSM-6610LV) equipped with energy-dispersive X-ray spectroscopy (EDS).

Optical characterization was performed using an Edinburgh Instruments FS5 spectrofluorometer equipped with a 150 W xenon lamp for excitation–emission measurements. Luminescence lifetimes were measured by time-correlated single-photon counting (TCSPC). To obtain radiative transition probabilities and oscillator strengths, Judd–Ofelt (J–O) analysis was conducted based on room- andhigh-temperature emission spectra.

This comprehensive methodology, paralleling our earlier Dy^{3+} study while tailored for Eu^{3+} doping, enables a direct comparison of host–dopant interactions and provides deeper insight into the red-emitting properties of $LaMgB_5O_{10}:Eu^{3+}$.

3. Results and discussions

3.1. XRD and rietveld refinement

To assess the phase purity and structural evolution of Eu^{3+}-doped $LaMgB_5O_{10}$ (LMBO) phosphors, powder X-ray diffraction (XRD) was conducted for all compositions within the 2θ range of 10–80°. As

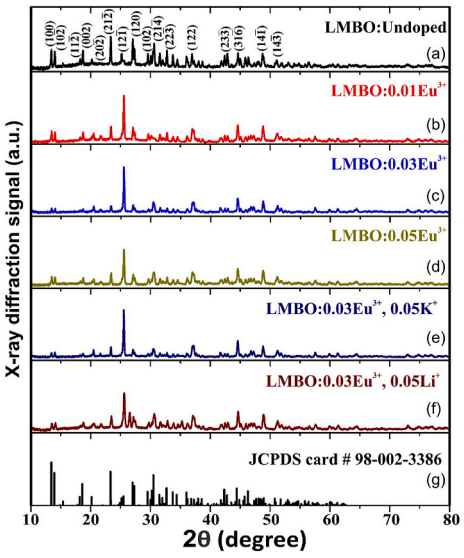

(a)

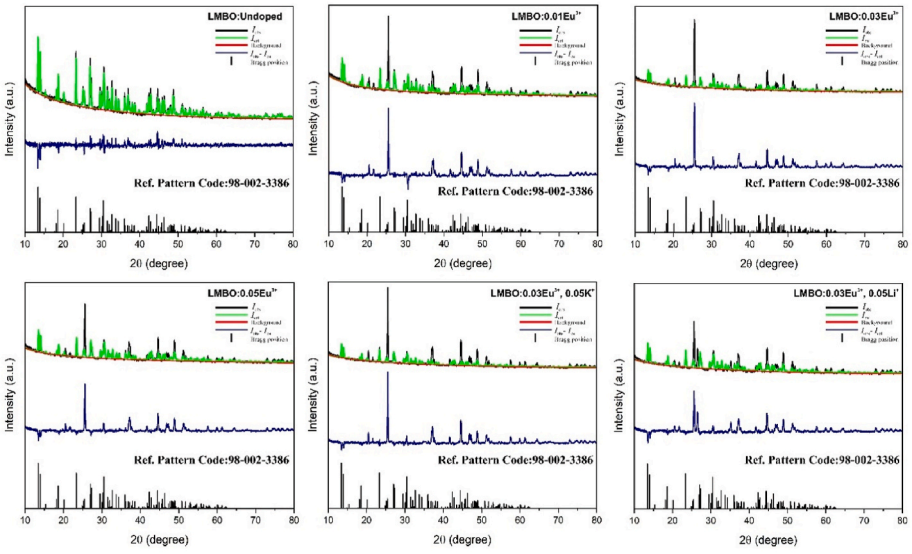

(b)

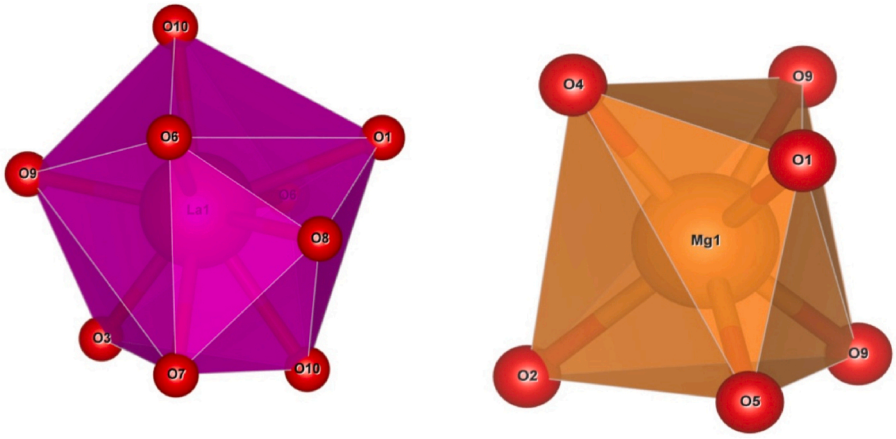

(c)

(caption on next page)

Fig. 1. (a) Powder X-ray diffraction patterns of undoped, Eu^{3+}-doped, and alkali co-doped $LaMgB_5O_{10}$ (LMBO:xEu^{3+}, yA^+; A = K^+, Li^+) samples recorded in the 2θ range of 10–80°. All reflections match well with the standard monoclinic LMBO phase (JCPDS #98-002-3386), indicating high crystallinity and phase purity with no secondary phases detected. (b) Rietveld refinement profiles for representative compositions. (c) Polyhedral representations of La (left) and Mg (right) coordination environments in the LMBO crystal structure, showing LaO_9 and MgO_6 units.

Table 1
Refined lattice parameters (*a*, *b*, *c*, β), unit cell volumes, and Rietveld reliability factors (χ^2, R_p, R_{wp}, R_{exp}) for undoped, Eu^{3+}-doped, and co-doped $LaMgB_5O_{10}$ samples.

	LMBO					
Unit Cell	Undoped	0.01Eu^{3+}	0.03Eu^{3+}	0.05Eu^{3+}	0.03Eu^{3+},0.05K^+	0.03Eu^{3+},0.05Li^+
a [Å]	8.78505	8.78821	8.79359	8.79676	8.78938	8.79310
b [Å]	7.61017	7.60793	7.61118	7.61005	7.60823	7.60855
c [Å]	12.64004	12.65061	12.65783	12.67141	12.64991	12.66522
beta [°]	13.5318	131.5637	131.6254	131.6011	131.6219	131.5757
Vol. [Å^3]	632.6011	632.8595	633.2728	634.3254	632.3628	633.8768
χ^2	2.369	5.861	6.061	4.960	6.271	5.509
R_p	0.064	0.135	0.155	0.126	0.155	0.139
R_{wp}	0.090	0.208	0.233	0.184	0.234	0.201
R_{exp}	0.038	0.035	0.038	0.037	0.037	0.036

depicted in Fig. 1a, all diffraction peaks for undoped, Eu^{3+}-doped, and co-doped (K^+, Li^+) LMBO samples can be unambiguously indexed to the monoclinic phase of $LaMgB_5O_{10}$ (space group $P2_1/c$), in accordance with the reference card JCPDS #98-002-3386. Moreover, these patterns are in close agreement with previous reports on LMBO doped with other rare-earth ions, including Ce^{3+} and Sm^{3+}, which exhibit similar peak positions and intensities, further substantiating the phase stability across various RE^{3+} substitutions (Hakami et al., 2025; Sakirzanovas et al., 2011). No impurity phases or amorphous backgrounds were detected, confirming high phase purity and the successful incorporation of dopants into the host matrix.

Subtle yet systematic shifts in peak positions were observed upon Eu^{3+} doping—particularly near reflections such as (100), (121), and (222)—which are indicative of lattice distortion caused by ionic substitution. A noticeable deviation in the (121) reflection is evident between the undoped and Eu^{3+}-doped LMBO samples, as well as with respect to the standard PDF card. This deviation can be ascribed to local lattice distortions and strain introduced by the substitution of La^{3+} with slightly smaller Eu^{3+} ions, which preferentially affect certain crystallographic planes. In addition, minor discrepancies with the reference PDF card may also arise from instrumental factors (e.g., calibration and sample displacement) and microstructural effects such as crystallite size and local defects, thus confirming that the deviation is not associated with secondary or impurity phases. These changes are consistent with the replacement of La^{3+} ions (1.216 Å, CN = 9) with slightly smaller Eu^{3+} ions (1.12 Å, CN = 9), resulting in a marginal contraction of the unit cell. In contrast, no significant shifts were observed around peaks sensitive to Mg^{2+} coordination, suggesting that Eu^{3+} does not substitute at the Mg site. This observation aligns well with previous findings in Dy^{3+}-doped LMBO, where similar rightward peak shifts (especially near $2\theta \approx 23.5°$) were reported due to substitution of La^{3+} (1.216 Å) by smaller Dy^{3+} ions (1.027 Å), as confirmed through XRD and Rietveld refinement (Hakami et al., 2025). Such consistency reinforces the structural robustness of the LMBO host in accommodating various trivalent rare-earth dopants without phase disruption.

Table 2
Ionic radii (R_m and R_d) and calculated ionic radius mismatch percentages (D_r) for Eu^{3+} substitution at Mg^{2+} and La^{3+} sites in LMBO, assuming equivalent coordination numbers (CN).

	Mg		Eu	
Dr	Rm	CN	Rm	CN
31.52	0.72	6	0.947	6
	La		Eu	
Dr	Rm	CN	Rm	CN
7.89	1.216	9	1.12	9

To further validate these structural changes, Rietveld refinement was performed on all samples using *HighScore Plus* software. The refinement profiles shown in Fig. 1b exhibit excellent agreement between observed and calculated patterns, as evidenced by low R_{wp} and χ^2 values across all compositions (Table 1). For the undoped sample, R_{wp} and χ^2 were 0.090 and 2.369, respectively; these values remained within acceptable limits for all doped variants. The goodness-of-fit indicators confirmed that the monoclinic crystal symmetry was preserved upon doping, with no structural degradation.

These changes are consistent with the replacement of La^{3+} ions (1.216 Å, CN = 9) with slightly smaller Eu^{3+} ions (1.12 Å, CN = 9), resulting in a marginal contraction of the unit cell.

Rietveld refinement of the Eu^{3+}-doped LMBO samples yielded excellent fits, as reflected by low R_{wp} and R_{exp} values (see Fig. 1b and c and Table 1). The undoped sample exhibited lattice parameters of a = 8.78505 Å, b = 7.61017 Å, c = 12.64004 Å, and β = 13.5318°, consistent with the monoclinic $P2_1/c$ space group. Upon 5 wt% Eu^{3+} substitution, the unit cell parameters showed a slight expansion to a = 8.79676 Å and c = 12.67141 Å, with a marginal increase in unit cell volume from 632.6011 Å^3 to 634.3254 Å^3. This behavior is attributed to the replacement of La^{3+} (1.216 Å, CN = 9) with slightly smaller Eu^{3+} ions (1.12 Å, CN = 9), inducing minimal structural distortion. Unlike Dy^{3+}-doped LMBO, where the substitution by smaller Dy^{3+} (1.027 Å) led to a minor contraction of the unit cell (Hakami et al., 2025), the Eu^{3+}-doped system exhibits a subtle volumetric expansion, indicating a more size-compatible incorporation. These findings suggest that Eu^{3+} can be effectively accommodated in the LMBO lattice while preserving its monoclinic symmetry and phase purity. Such consistency between the present Eu^{3+}-doped system and previously reported Dy^{3+}-doped LMBO (Hakami et al., 2025) reinforces the structural resilience of the LMBO lattice toward accommodating trivalent rare-earth dopants without inducing phase transformation or severe distortion.

The subtle expansion of the unit cell upon Eu^{3+} substitution, despite its slightly smaller ionic radius compared to La^{3+}, may be attributed to local lattice distortions, strain relaxation effects, or the presence of charge-compensation mechanisms introduced during doping. Such structural relaxation phenomena are common in rare-earth-doped borates and can lead to slight deviations from the purely ionic-radius-based expectations.

The refined lattice parameters revealed a gradual and composition-dependent variation. Specifically, the unit cell volume increased slightly from 632.6011 Å^3 (undoped) to 634.3254 Å^3 for the 0.05Eu^{3+}-doped sample. Such expansion, although modest, is consistent with the expected lattice strain induced by the substitution of Eu^{3+} into La^{3+} sites. In co-doped samples, the volume changes were more complex and

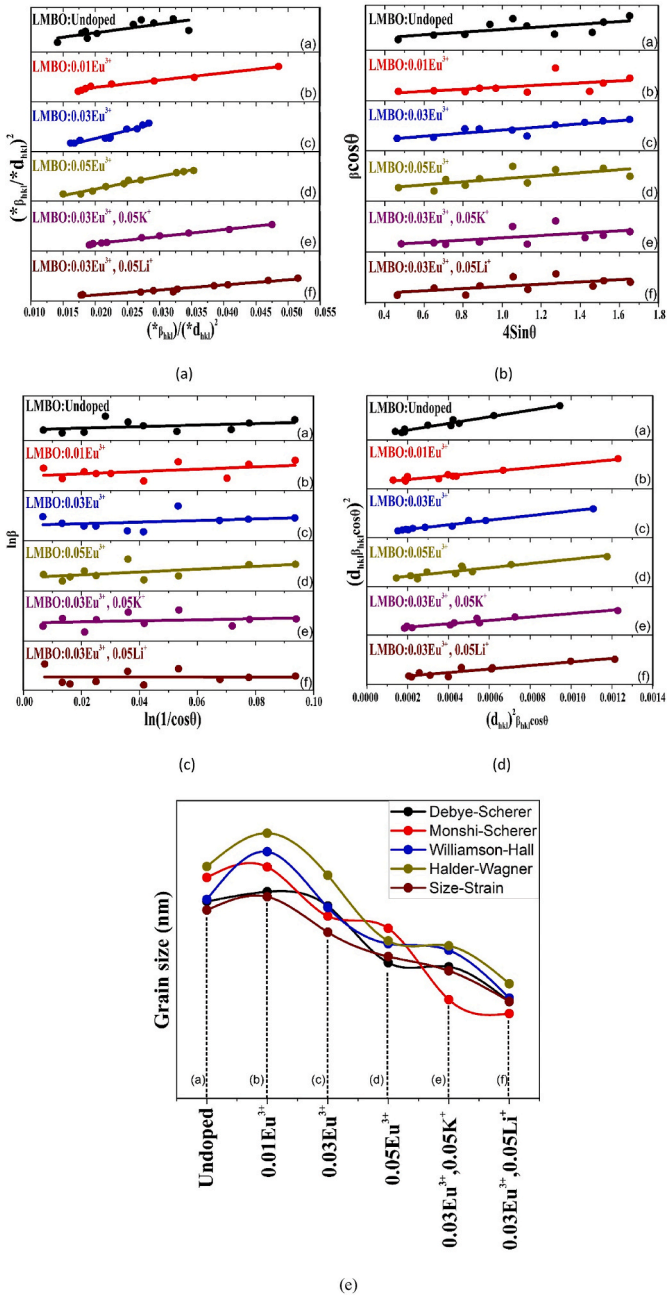

Fig. 2. (a) Halder-Wagner, (b) Williamson-Hall, (c) Monshi-Scherrer, and (d) Size–Strain plots for LMBO:Undoped, LMBO:0.01Eu^{3+}, LMBO:0.03Eu^{3+}, LMBO:0.05Eu^{3+}, LMBO:0.03Eu^{3+},0.05K^{+}, and LMBO:0.03Eu^{3+},0.05Li^{+} samples. Each plot represents the linear fitting used to estimate crystallite size and strain based on different theoretical models. (e) Comparison of crystallite sizes calculated by five different methods—Debye-Scherrer, Monshi-Scherrer, Williamson-Hall, Halder-Wagner, and Size–Strain—for LMBO:Undoped, LMBO:0.01Eu^{3+}, LMBO:0.03Eu^{3+}, LMBO:0.05Eu^{3+}, LMBO:0.03Eu^{3+},0.05K^{+}, and LMBO:0.03Eu^{3+},0.05Li^{+} samples.

varied with the ionic radius of the co-dopant, suggesting a combined effect of aliovalent substitution and charge compensation.

To elucidate the dopant incorporation mechanism, the ionic radius mismatch percentage (D_r) was calculated using the following formula, according to Shannon (1976):

$$D_r = \left| \frac{R_m(CN) - R_d(CN)}{R_m(CN)} \right| \quad (1)$$

where R_m and R_d represent the ionic radii of the host and dopant ions, respectively, for the same coordination number (CN). As summarized in Table 2, the D_r value for Eu^{3+}→La^{3+} substitution is 7.89 %, which is significantly below the 30 % threshold commonly considered acceptable for substitutional doping (Ling-Hu et al., 2024). In contrast, the D_r for Eu^{3+}→Mg^{2+} substitution reaches 31.52 %, exceeding the permissible limit, thus making this substitution site energetically unfavorable. These results confirm that Eu^{3+} preferentially occupies La^{3+} sites.

The coordination environments of La and Mg cations, visualized via polyhedral representations in Fig. 1c, further support this conclusion. La^{3+} is coordinated by nine oxygen atoms in a distorted tricapped trigonal prismatic geometry, while Mg^{2+} adopts a regular octahedral (CN = 6) coordination. The larger coordination number and spatial accommodation around La^{3+} sites are more favorable for incorporating Eu^{3+} ions without significant local distortion, whereas Mg^{2+} sites are sterically restrictive and electrostatically incompatible with Eu^{3+}.

Collectively, these results from Rietveld refinement, lattice parameter analysis, ionic radius mismatch evaluation, and local coordination geometry confirm that Eu^{3+} ions are effectively incorporated into the LMBO lattice via substitution at the La^{3+} site. The structural robustness of the host framework is maintained across all doped and co-doped samples, providing a reliable platform for subsequent optical investigations.

3.1.1. *Crystallite size and strain analysis*

Following the phase identification and lattice parameter refinement discussed in Section 3.1, crystallite size and microstrain analyses were conducted to further understand the structural impact of Eu^{3+} doping and alkali co-doping on the LMBO matrix. Four models were employed: the Halder–Wagner method (Hepp and Baerlocher, 1988), which uses a Voigt function to separate size and strain effects with enhanced sensitivity to low and intermediate diffraction angles; the Williamson–Hall method (Williamson and Hall, 1953), which assumes uniform strain and plots βcosθ versus 4sinθ to extract crystallite size and strain; the Monshi–Scherrer approach (Monshi et al., 2012), which linearizes the traditional Scherrer formula using lnβ versus ln(1/cosθ), allowing better data fitting and quality control via slope analysis; and the Size–Strain Plot (SSP) method (Diputra et al., 2025), which reduces error propagation by treating size and strain contributions independently in a weighted plot. The corresponding linear fittings are shown in Fig. 2a–d, respectively. Each method provides unique assumptions about the distribution of strain and crystallite orientation. For example, the Williamson–Hall model assumes uniform strain distribution, while the Halder–Wagner approach accounts for strain broadening and is considered more accurate for anisotropic systems. The Monshi–Scherrer method adapts the classical Scherrer equation into a log–log format to improve linearity, and the SSP method minimizes error propagation by plotting strain and size effects separately. Across all methods, a general trend of decreasing crystallite size was observed with increasing Eu^{3+} concentration, attributed to lattice distortion induced by the ionic radius mismatch between La^{3+} (1.216 Å, CN = 9) and Eu^{3+} (1.12 Å, CN = 9). Notably, the introduction of alkali co-dopants (K^{+} and Li^{+}) resulted in further size reduction, likely due to additional charge compensation and lattice strain effects. The comparative crystallite sizes obtained from each model are summarized in Fig. 2e, revealing consistency in trends despite numerical variation across methods. Among them, the Halder–Wagner model consistently yielded the largest grain sizes, while the Monshi–Scherrer method produced slightly lower values due to its inherent assumptions. A consolidated comparison of crystallite size and strain values for all doped and co-doped compositions is provided in Table 3, illustrating the effectiveness of each method in capturing microstructural variations.

These results confirm that rare-earth doping and aliovalent co-doping lead to a measurable impact on crystallite size and strain, offering important insights into tailoring the structural properties of LMBO phosphors for enhanced optical behavior. These microstructural

Table 3
Crystallite size (D) and microstrain (ε) values of LMBO:Undoped, Eu^{3+}-doped, and Eu^{3+}/alkali co-doped samples calculated using different models: Debye-Scherrer, Monshi-Scherrer, Williamson-Hall, Halder-Wagner, and Size–Strain methods.

		LMBO					
Concentration		Undoped	$0.01Eu^{3+}$	$0.03Eu^{3+}$	$0.05Eu^{3+}$	$0.05Eu^{3+}$,$0.01K^{+}$	$0.05Eu^{3+}$,$0.01Li^{+}$
Debye-Scherer	D (nm)	82.407	84.111	81.607	71.866	70.994	64.890
	$\delta \times 10^{-3}$ (nm^{-2})	0.1472	0.1413	0.1501	0.1396	0.1984	0.2374
Monshi-Scherrer	D (nm)	86.584	88.421	79.838	77.689	65.254	62.802
	$\delta \times 10^{-3}$ (nm^{-2})	0.1333	0.1279	0.1569	0.1656	0.2348	0.2535
Williamson-Hall	D (nm)	82.752	91.079	81.357	75.034	73.885	65.527
	$\varepsilon \times 10^{-3}$	1.76	2.09	1.55	1.93	2.20	2.69
Halder-Wagner	D (nm)	88.495	94.339	86.956	75.519	74.626	68.027
	$\varepsilon \times 10^{-3}$	8.88	9.95	10.29	10.76	9.41	14.46
Size-Strain	D (nm)	80.903	83.227	77.030	72.772	70.299	64.940
	$\varepsilon \times 10^{-3}$	1.51	1.80	1.27	1.64	1.67	1.73

modifications are anticipated to influence not only the phase purity but also the optical and functional properties of the LMBO materials, as will be discussed in subsequent sections.

3.1.2. Vibrational analysis (FTIR and Raman spectroscopy)

To complement the structural analysis from XRD, vibrational spectroscopy techniques—FTIR and Raman—were employed to investigate the local bonding environments and short-range order within the LMBO lattice. These techniques are particularly effective in detecting the characteristic modes of borate units, which are sensitive to structural distortion induced by dopant incorporation.

The FTIR spectra of undoped and Eu^{3+}/alkali-doped LMBO samples are shown in Fig. 3a. All spectra exhibit well-defined vibrational bands typically associated with borate groups. The prominent absorption bands in the region of 1300–800 cm^{-1} are attributed to the asymmetric and symmetric stretching vibrations of the BO_3 and BO_4 units, in accordance with previous literature reports (Boda et al., 2016; Hakami et al., 2025; Sakirzanovas et al., 2011; Xiang et al., 2022). The broad band around 3450 cm^{-1} is assigned to O–H stretching, indicative of surface-adsorbed moisture or residual hydroxyl groups, while the corresponding bending vibration appears near 1630 cm^{-1}. Importantly, a slight shift in the B–O stretching bands is observed with increasing Eu^{3+} concentration, suggesting local lattice distortion due to ionic substitution and charge compensation effects. Co-doping with K^{+} or Li^{+} induces further shifts and noticeable peak broadening, a behavior consistent with earlier studies on alkali-modified borate glasses, where the introduction of alkali ions was shown to modify the borate network through the creation of non-bridging oxygens and changes in BO_3/BO_4 connectivity (Balachander et al., 2013).

The Raman spectra of undoped and Eu^{3+}/alkali-doped LMBO samples are shown in Fig. 3b. All samples exhibit the characteristic vibrational features of borate lattices, with prominent peaks corresponding to B–O stretching and bending modes. The bands in the 1300–800 cm^{-1} region are attributed to the asymmetric and symmetric vibrations of BO_3 and BO_4 groups, consistent with earlier reports on borate frameworks (Sakirzanovas et al., 2011; Somaily et al., 2025). Lower-frequency modes near 460 cm^{-1} and 360 cm^{-1} are assigned to bending vibrations and external lattice modes, as commonly observed in borate-type materials (Gharavi-Naeini et al., 2018). Compared to the undoped LMBO, both Eu^{3+}-doped and co-doped samples show minor shifts and intensity variations in these Raman peaks, which are indicative of subtle structural rearrangements at the local level. Such peak broadening and frequency shifts have also been reported in alkali-modified borate systems, where the introduction of K^{+} or Li^{+} ions perturbs the borate network by altering BO_3/BO_4 connectivity and generating non-bridging oxygens (Balachander et al., 2013). Overall, the combined FTIR and Raman analyses confirm the coexistence of BO_3 and BO_4 groups in the LMBO framework and demonstrate that rare-earth and alkali doping induce measurable modifications in the vibrational behavior of the host lattice. These findings support the structural observations obtained from XRD and suggest that dopant-induced distortions are accommodated without disrupting the overall borate framework.

3.1.3. Morphological and compositional analysis (SEM–EDS)

The elemental composition and morphology of undoped and Eu^{3+}-doped LMBO samples were investigated using SEM–EDS, and the results are presented in Fig. 4. For the undoped LMBO sample, the EDS spectrum shows the expected elemental peaks of La, Mg, B, and O, in good agreement with the nominal composition. Upon Eu^{3+} incorporation (3 wt%), additional peaks corresponding to Eu were clearly observed, confirming the successful substitution of Eu^{3+} ions into the LMBO lattice. The measured Eu content was ~3.2 wt%, which is in close agreement with the nominal loading. Such consistency indicates a relatively homogeneous distribution of Eu^{3+} within the sampling region, although minor deviations may still occur due to the semi-quantitative nature of EDS and localized probe volume effects.

Morphological examination further reveals that the undoped LMBO sample exhibits irregularly shaped, plate-like grains with relatively smooth surfaces. In contrast, the Eu^{3+}-doped LMBO shows a more porous and agglomerated microstructure, with particles displaying rougher surfaces and partial grain coalescence. Such modifications are frequently observed upon rare-earth doping and are attributed to the ionic radius mismatch between La^{3+} (1.16 Å, CN = 8) and Eu^{3+} (1.066 Å, CN = 8), which introduces localized strain and alters grain growth dynamics during solid-state synthesis. Similar morphological changes have been reported for Eu^{3+}-doped borates and aluminates, where dopant incorporation affects nucleation and densification behavior (Boda et al., 2016; Gharavi-Naeini et al., 2018). Overall, the combined EDS and SEM results provide direct evidence of Eu incorporation into the LMBO lattice and highlight the impact of Eu^{3+} substitution on both the chemical composition and microstructural evolution of the host material.

3.2. Photoluminescence studies

3.2.1. Photoluminescence excitation (PLE) and emission behavior

The excitation spectrum of LMBO:Eu^{3+} monitored at 609 nm (Fig. 5a) exhibits two characteristic features: a broad absorption band in the UV region (220–300 nm) and several sharp, well-resolved lines in the visible range. The broad band is attributed to $O^{2-} \rightarrow Eu^{3+}$ charge-transfer transitions (CTBs), arising from ligand-to-metal charge transfer between O 2p orbitals and the empty 4f states of Eu^{3+} (Hong et al., 2022). Such CTBs are a common fingerprint of Eu^{3+} in oxide and borate hosts, and their position is known to vary with the covalency and coordination geometry of the host lattice. In addition, sharp lines corresponding to intra-configurational 4f–4f transitions are observed; although parity is forbidden in free Eu^{3+} ions, they become partially allowed in solids through crystal-field and odd-parity phonon mixing. These narrow f–f features serve as sensitive probes of the local symmetry and crystal-field strength at Eu^{3+} sites, complementing the information

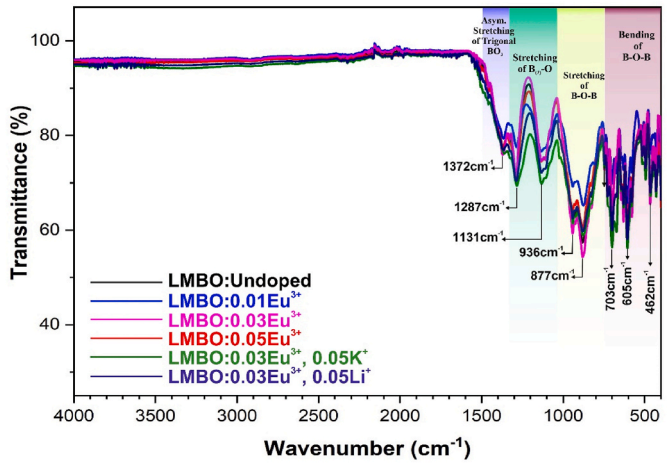

(a)

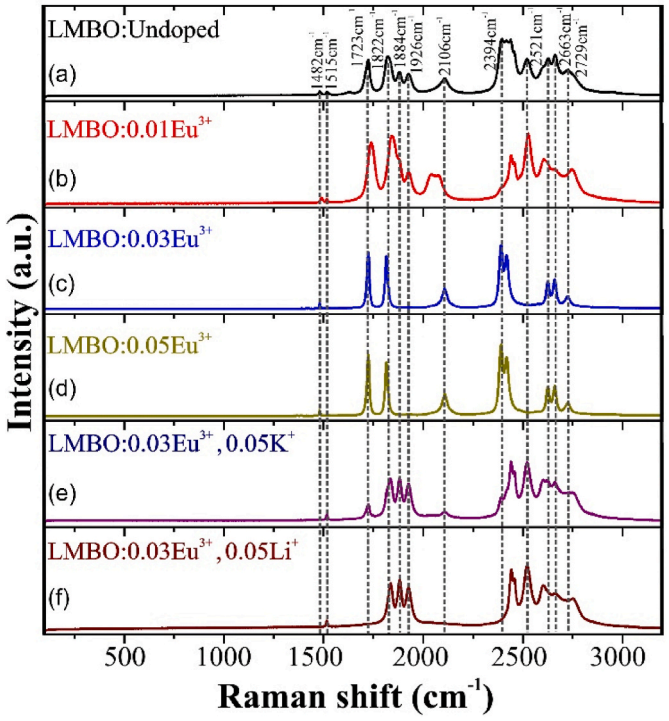

(b)

Fig. 3. (a) FTIR spectra of undoped, Eu^{3+}-doped, and Eu^{3+}/alkali (K^+, Li^+) co-doped LMBO samples (b) Raman spectra of the same samples, highlighting BO_3/BO_4 stretching and low-frequency lattice modes (~460 and 360 cm^{-1}).

provided by the CTB. The most intense resonance corresponds to the $^7F_0 \rightarrow {}^5L_6$ transition (~392 nm), accompanied by well-defined peaks at ~463 nm ($^7F_0 \rightarrow {}^5D_2$) and weaker features at ~412 nm ($^7F_0 \rightarrow {}^5D_3$) and ~523–531 nm ($^7F_0 \rightarrow {}^5D_1/{}^5D_0$). These assignments are in good agreement with previous spectroscopic studies of Eu^{3+}-doped borates and related oxide hosts (George et al., 2025; Somaily et al., 2025).

Upon excitation at 393 nm, the emission spectrum of LMBO:Eu^{3+} (Fig. 5b) is dominated by the characteristic red band at ~609 nm, corresponding to the forced electric dipole transition $^5D_0 \rightarrow {}^7F_2$. The prominence of this hypersensitive transition confirms that Eu^{3+} ions occupy sites of low inversion symmetry within the LMBO lattice. In addition to the dominant red line, the magnetic dipole transition $^5D_0 \rightarrow {}^7F_1$ appears at ~591 nm, together with weaker features at 649 nm ($^5D_0 \rightarrow {}^7F_3$) and in the far-red region near 690–700 nm ($^5D_0 \rightarrow {}^7F_4$) (Altowyan et al., 2024; Jabali et al., 2024; Somaily et al., 2025).

The asymmetry ratio ($R = I(^5D_0 \rightarrow {}^7F_2)/I(^5D_0 \rightarrow {}^7F_1)$) was evaluated as a function of Eu^{3+} concentration in LMBO (Fig. 5c). The R values ranged between ~3.55 and 4.34, with the maximum ($R \approx 4.34$) obtained at 0.02 wt% Eu^{3+}, suggesting that at this concentration the Eu^{3+} ions experience the strongest local asymmetry. At higher concentrations (e.g., 0.03 wt%), although the overall emission intensity was maximized, the asymmetry ratio decreased slightly (~3.65), indicating a partial relaxation of site distortion. Such decoupling between the integrated PL intensity and the R value is common in Eu^{3+}-doped oxides and borates, since the emission strength is jointly determined by absorber population and non-radiative processes, whereas the R parameter is primarily sensitive to the local coordination geometry (Blasse and Grabmaier, 1994; Boda et al., 2016; Sakirzanovas et al., 2011). These results highlight that LMBO provides a strongly asymmetric environment for Eu^{3+}, and subtle variations in local site symmetry occur with increasing dopant concentration.

A particularly notable feature of our spectra is the relatively intense far-red emission band (~700 nm, $^5D_0 \rightarrow {}^7F_4$). While this transition is typically weak in highly symmetric lattices, its enhancement in LMBO indicates the presence of local structural distortions that lower the site symmetry of Eu^{3+} (Altowyan et al., 2025a). Similar anomalous intensity has also been reported in Eu^{3+}-doped Na_2ZnSiO_4, where a strong 702 nm emission was attributed to distorted local coordination and site asymmetry (Liu et al., 2019). This parallel suggests that LMBO provides a comparable environment favoring enhanced far-red emission, thereby broadening its potential for optoelectronic applications requiring extended red or far-red output. Since Eu^{3+} ions substitute isovalently for La^{3+} without requiring charge compensation, the observed effect is more plausibly associated with subtle lattice mismatches arising from the smaller ionic radius of Eu^{3+} compared to La^{3+}, as well as variations in the local Eu–O coordination geometry. These distortions modify the crystal field around Eu^{3+} and promote stronger electric dipole activity in the far-red region.

To further explore the excitation-dependent behavior of Eu^{3+} in LMBO, emission spectra were recorded under multiple excitation wavelengths (316, 360, 375, 392, and 463 nm), as shown in Fig. 5b. In all cases, the emission profiles are dominated by the characteristic $^5D_0 \rightarrow {}^7F\_J$ transitions (J = 0–6), with the most intense band centered at ~609 nm ($^5D_0 \rightarrow {}^7F_2$). The overall spectral shape remains nearly unchanged, confirming that the Eu^{3+} ions occupy similar crystallographic sites regardless of the excitation pathway. However, clear variations in emission intensity are observed depending on the excitation wavelength. In particular, the strongest luminescence arises under 392 nm excitation, which corresponds to the $^7F_0 \rightarrow {}^5L_6$ transition of Eu^{3+}. This agrees well with previous reports identifying $^5L_6$ as the most efficient absorption channel in Eu^{3+}-activated borates and oxides (Blasse and Grabmaier, 1994; Mitina et al., 2023). By contrast, excitations at 316 and 360 nm ($^7F_0 \rightarrow {}^5H_6$, $^7F_0 \rightarrow {}^5D_4$) yield comparatively weaker emissions, reflecting the lower oscillator strength of these transitions. The 463 nm excitation, corresponding to the $^7F_0 \rightarrow {}^5D_2$ absorption, also produces visible red emission but with reduced intensity, consistent with its narrower absorption cross-section. Such excitation-dependent emission behavior highlights the importance of selecting appropriate excitation channels for optimizing emission efficiency in photonic applications (Jayakiruba et al., 2017; Mitina et al., 2023).

3.2.2. *Concentration quenching and the evolution of the far-red $^5D_0 \rightarrow {}^7F_4$ band*

Under 392 nm excitation, the integral PL intensity of LMBO:xEu^{3+} increases with Eu^{3+} content up to x = 3 wt% and then decreases for x ≥ 5 wt%, evidencing concentration quenching (Fig. 6). In Eu^{3+}-activated hosts, the quenching is commonly attributed to non-radiative energy migration among neighboring Eu^{3+} ions followed by trapping at defects or killer centers, with the transfer mediated predominantly by

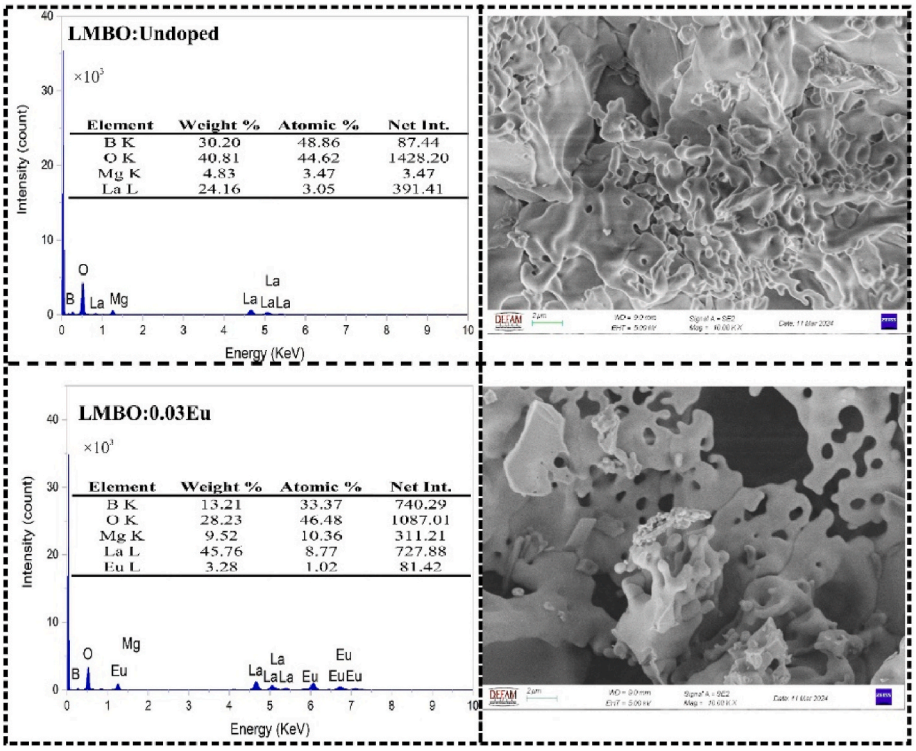

Fig. 4. SEM micrographs and EDS spectra of (a) undoped LMBO and (b) Eu^{3+}-doped LMBO (3 wt%).

multipolar interactions (dipole–dipole/dipole–quadrupole. To rationalize the quenching threshold, we estimated the critical transfer distance using Blasse's relation (Blasse, 1968):

$$R_c = 2\left[\frac{3V}{4\pi x_c N}\right]^{1/3} \quad (2)$$

where V is the unit-cell volume, x_c is the critical Eu^{3+} site fraction, and N is the number of Eu-substitutable cation sites per unit cell. From Rietveld refinement at 3 wt% Eu^{3+}, the refined unit-cell volume was found to be V = 633.27 Å^3. Since Eu^{3+} ions substitute for La^{3+} in LMBO, the number of available La^{3+} sites per unit cell is taken as N = 4. With an optimum concentration of $x_c \approx 0.03$, the calculated critical distance was $R_c \approx 12.3$ Å. This value is significantly larger than the 5 Å empirical limit for short-range exchange interactions (Dexter, 1953), confirming that the concentration quenching in LMBO:Eu^{3+} is predominantly governed by quadrupole-quadrupole, in line with recent analyses of Eu^{3+}-activated borates and oxides (K. et al., 2025; Kaynar et al., 2024; Sekrafi et al., 2025; Shablinskii et al., 2023).

The evolution of emission intensity with Eu^{3+} concentration in LMBO was analyzed to clarify the quenching mechanism. The photoluminescence intensity initially increases with Eu^{3+} loading, reaching a maximum at 3 wt%, before decreasing for higher concentrations (≥5 wt %), consistent with concentration quenching behavior (Fig. 6b). To probe the dominant interaction type, the Dexter–Inokuti framework was employed:

$$log\left(\frac{I}{x}\right) = -\frac{\theta}{3}log(x) + c \quad (3)$$

where the interaction parameter θ distinguishes between dipole–dipole (θ = 6), dipole–quadrupole (θ = 8), and quadrupole–quadrupole (θ = 10) coupling. Fitting the quenching region yielded a slope of −3.45, corresponding to θ ≈ 10, which identifies quadrupole–quadrupole interactions as the dominant non-radiative pathway. This is consistent with the large R_c (~12.3 Å) which rules out short-range exchange coupling.

Quadrupole–quadrupole dominated quenching has also been reported in other Eu^{3+}-doped borates and related oxide hosts. For example, Gaikwad et al. (2025) recently demonstrated θ ≈ 10 in a borate-based Eu^{3+} phosphor, confirming the prevalence of quadrupole–quadrupole coupling in systems where rare-earth sites are widely separated by polyborate units. Such parallels reinforce that in LMBO, long-range multipolar interactions, rather than short-range exchange, govern the quenching behavior at higher Eu^{3+} loadings. Quadrupole–quadrupole dominated quenching has also been reported in other Eu^{3+}-doped borates and related oxide hosts. For example, Gaikwad et al. (2025) recently demonstrated θ ≈ 10 in a borate-based Eu^{3+} phosphor, confirming the prevalence of quadrupole–quadrupole coupling in systems where rare-earth sites are widely separated by polyborate units. Such parallels reinforce that in LMBO, long-range multipolar interactions, rather than short-range exchange, govern the quenching behavior at higher Eu^{3+} loadings.

A more detailed, dynamics-focused view assigns the decrease in PL to the increase of inter-ion energy transfer (ET) rates, which arises from Dexter-type electronic coupling or long-range Coulombic coupling, which outcompetes radiative decay as the Eu^{3+}–Eu^{3+} separation shrinks. Kinetic modeling and time-resolved experiments corroborating this picture have been reported recently for lanthanide emitters (Spelthann et al., 2023; Tanner et al., 2022).

Far-red $^5D_0 \rightarrow {}^7F_4$ band (≈700 nm). A notable spectral feature in LMBO:xEu^{3+} is the relative enhancement of the $^5D_0 \rightarrow {}^7F_4$ line with increasing Eu^{3+} content (Fig. 6a), even when the total PL starts to quench. This behavior does not contradict the intensity drop of the whole spectrum; rather, it indicates a redistribution of oscillator strength among $^5D_0 \rightarrow {}^7F_J$ channels driven by local-symmetry changes and J-mixing as the Eu–O coordination becomes more distorted at higher dopant loadings. Recent reports have shown anomalously strong $^5D_0 \rightarrow {}^7F_4$ emission in several Eu^{3+} hosts when Eu^{3+} occupies low-symmetry (e.g., distorted square-antiprismatic or D_2d-symmetry) sites, or when charge-compensation/defect chemistry modifies the crystal field; in such cases, the $^5D_0 \rightarrow {}^7F_4$ transition gains intensity relative to $^5D_0 \rightarrow {}^7F_2$ (Chi et al., 2018; Ling-Hu et al., 2024; Souadi et al., 2023).

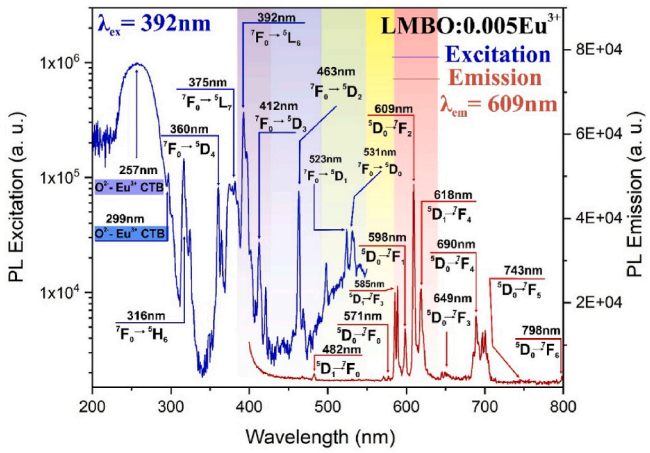

(a)

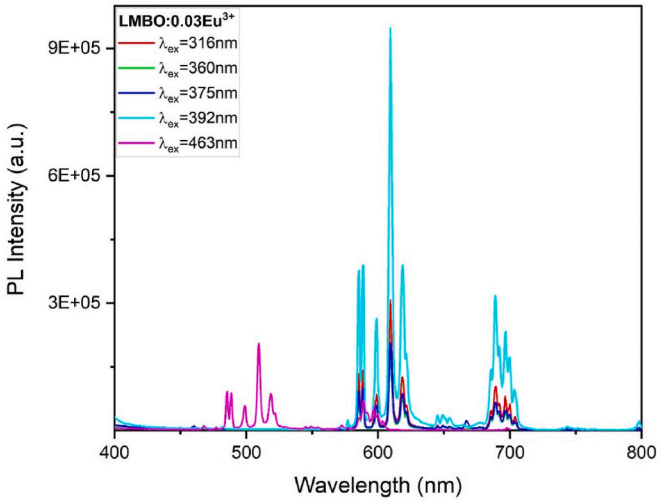

(b)

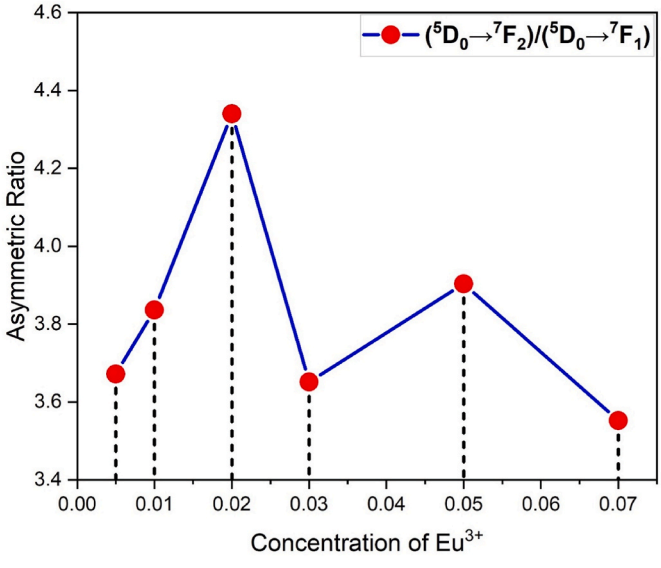

(c)

(caption on next column)

Fig. 5. (a) Photoluminescence excitation (PLE) spectrum of LMBO:Eu^{3+} monitored at 609 nm, showing the O^{2-}→Eu^{3+} charge-transfer band and characteristic 4f–4f transitions. (b) Emission spectra of LMBO:Eu^{3+} under different excitation wavelengths (316, 360, 375, 392, and 463 nm), dominated by the $^5D_0$→^7F_J transitions with the strongest red emission at ~609 nm. (c) Concentration dependence of the asymmetry ratio (R = I($^5D_0$→$^7F_2$)/I($^5D_0$→$^7F_1$)) for LMBO:Eu^{3+} phosphors. (For interpretation of the references to color in this figure legend, the reader is referred to the Web version of this article.)

In our LMBO matrix, Eu^{3+} substitutes isovalently for La^{3+}; thus, the far-red enhancement is most plausibly linked to subtle lattice-strain–induced distortions and energy migration toward more distorted Eu^{3+} sites as x increases. This spectral-weight shift toward $^5D_0$→$^7F_4$ can therefore coexist with (and even be accentuated by) global concentration quenching of the total emission—a trend that has also been highlighted in recent Eu^{3+} systems where the maximum PL output and the maximum site asymmetry (R) occur at different dopant levels (Morebodi et al., 2024).

3.2.3. *Influence of alkali co-doping (K^+/Li^+) on PL behavior*

The co-doping of Eu^{3+}-activated LMBO with alkali ions (Li^+, K^+) reveals clear differences in the evolution of the emission spectra. While the overall PL profiles remain dominated by the $^5D_0$→^7F_J transitions, both the integrated intensity and the relative band distribution are strongly modified depending on the nature and concentration of the co-dopant.

In the case of Li^+ incorporation, the overall enhancement is moderate but evident (Fig. 7a). For example, the peak area of the hypersensitive $^5D_0$→$^7F_2$ transition increases from 3.10×10^6 (Eu^{3+}) to 4.61×10^7 (Li^+), while the far-red $^5D_0$→$^7F_4$ transition rises from 1.69×10^6 to 4.02×10^7. This selective redistribution of oscillator strength indicates that Li^+ co-doping perturbs the Eu–O coordination environment, reducing the asymmetry that favors $^5D_0$→$^7F_2$ while simultaneously strengthening $^5D_0$→$^7F_4$. Similar behavior was reported by Souadi et al. (2023) and Chi et al. (2018), where distortions of Eu–O polyhedra suppressed $^5D_0$→$^7F_2$ but promoted anomalously strong $^5D_0$→$^7F_4$ emission.

By contrast, K^+ co-doping produces a markedly stronger enhancement compared to Li^+ (Fig. 7b). The $^5D_0$→$^7F_2$ band increases from 3.10×10^6 (Eu^{3+}) to 1.16×10^7 (K^+), while the $^5D_0$→$^7F_4$ band grows from 1.69×10^6 to 8.56×10^7, corresponding to more than a fivefold increase. This strong amplification is comparable to the ~8–10 × rise reported in garnet-type hosts (Chi et al., 2018) and aligns with the findings of Souadi et al. (2023) on Eu^{3+}-activated $ZnGa_2O_4$, where local distortion similarly promoted the $^5D_0$→$^7F_4$ transition.

The microscopic origin of this effect can be rationalized by considering more than just ionic radius mismatch. While smaller Li^+ (0.76 Å, CN = 6) and larger K^+ (1.52 Å, CN = 8) both introduce charge imbalance, the lattice strain, local phonon coupling, and site occupancy preference differ significantly. K^+ is more likely to expand the Eu–O polyhedra by lengthening Eu–O bonds, creating a coordination closer to distorted square antiprismatic (D_2d-like) symmetry, which strongly favors $^5D_0$→$^7F_4$ activation. Li^+, on the other hand, tends to induce stronger local strain but less efficient stabilization of expanded coordination, leading to weaker far-red enhancement.

The pronounced far-red anomaly in K^+ co-doped LMBO originates from extended Eu–O coordination, which optimizes bond lengths, reduces 4f–phonon overlap, and lowers site symmetry. Consequently, the parity-forbidden $^5D_0$→$^7F_4$ transition gains oscillator strength at the expense of $^5D_0$→$^7F_2$. Similar reasoning was invoked by Souadi et al. (2023), Ling-Hu et al. (2024), and Chi et al. (2018) to explain anomalously strong far-red emission in Eu^{3+}-activated hosts with distorted coordination geometries.

Collectively, these observations confirm that the alkali co-doping effect in LMBO cannot be reduced to a simple ionic size argument. Instead, it arises from a synergy of lattice strain, local phonon coupling, and coordination expansion, which together modulate the relative

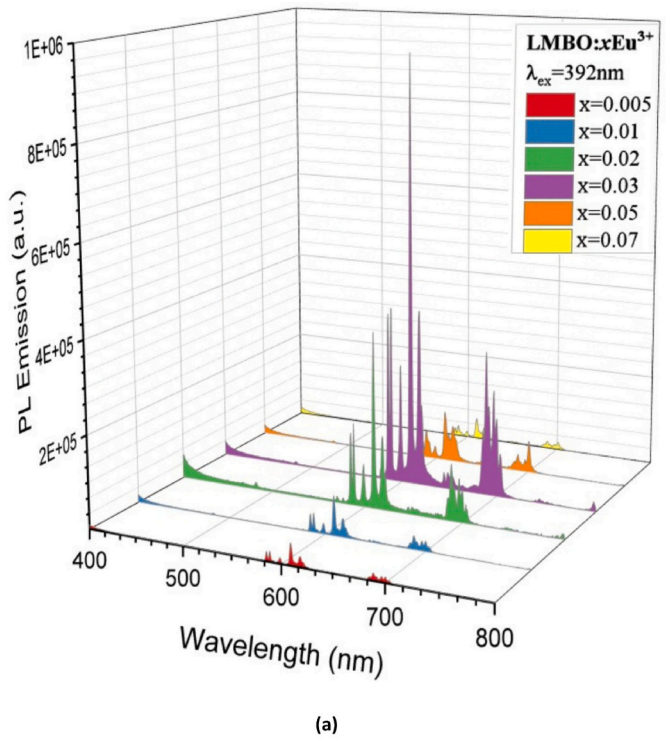

(a)

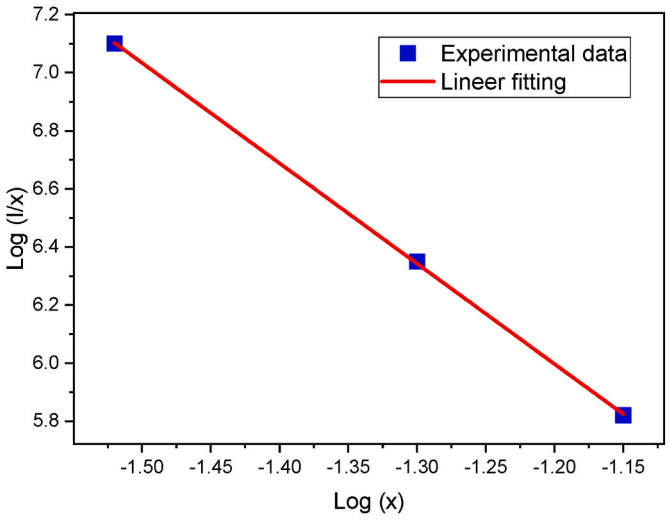

(b)

Fig. 6. (a) PL emission spectra of LMBO:xEu^{3+} (x = 0.005–0.07) under 392 nm excitation, showing maximum intensity at 3 wt% and concentration quenching at higher doping. (b) Dexter–Inokuti analysis of the quenching region, with a slope of −3.45 (θ ≈ 10).

strengths of Eu^{3+} emission channels. Among the alkali ions investigated, K^{+} proves uniquely effective in amplifying the far-red $^5D_0 \rightarrow {}^7F_4$ transition, establishing LMBO:Eu^{3+},K^{+} as a promising phosphor for applications requiring extended red and far-red emission, such as pc-wLEDs and plant growth lighting.

Although direct structural determination of alkali positions is not available from the present data, qualitative considerations can be made. Owing to its small ionic radius, Li^{+} is likely to occupy interstitial sites or partially substitute Mg^{2+}, thereby perturbing the Eu–O coordination and lowering the CTB energy, which promotes ATQ. In contrast, the larger K^{+} cation is more likely to reside in interstitial channels of the borate lattice. Its incorporation modifies the crystal-field asymmetry around Eu^{3+}, enhancing the oscillator strength of the far-red $^5D_0 \rightarrow {}^7F_4$ transition. Thus, the distinct roles of Li^{+} and K^{+} arise from their different lattice accommodation and local perturbations of Eu^{3+} coordination.

3.2.4. *Decay lifetime analysis of Eu^{3+} emission*

To further investigate the radiative processes, the decay curves of the $^5D_0$ level of Eu^{3+} ions were measured under 392 nm excitation and monitored at the $^5D_0 \rightarrow {}^7F_2$ transition (~612 nm). The decay profiles for different Eu^{3+} concentrations as well as for selected alkali co-doped samples are presented in Fig. 8. All curves deviate from a single-exponential behavior, indicating the presence of multiple decay channels associated with energy transfer, cross-relaxation, and structural inhomogeneity in the LMBO host lattice.

The experimental decay data were well fitted by a tri-exponential function

$$I(t) = A_1\, exp\left(-\frac{t}{\tau_1}\right) + A_2\, exp\left(-\frac{t}{\tau_2}\right) + A_3\, exp\left(-\frac{t}{\tau_2}\right) \quad (4)$$

where A_i are the amplitude fractions and τ_i are the decay components. The average lifetime was obtained using:

$$\tau_{avg} = \frac{\sum_i A_i \tau_i^2}{\sum_i A_i \tau_i} \quad (5)$$

The fitting parameters are summarized in Table 4. The average lifetime decreases slightly with increasing Eu^{3+} content, consistent with concentration quenching via enhanced multipolar interactions (e.g., τ_{avg} = 1.38 ms at 0.03Eu^{3+}, reduced to 1.31 ms at 0.05Eu^{3+}).

For alkali co-doped samples, distinct behaviors are observed. Li^{+} incorporation generally leads to shorter lifetimes ($\tau_{avg} \approx$ 0.87–1.36 ms), which can be attributed to stronger local distortion and the introduction of additional non-radiative channels. By contrast, K^{+} co-doping yields intermediate values (τavg ≈ 0.94–1.13 ms), indicating that the strong enhancement of far-red emission arises primarily from oscillator strength redistribution rather than prolonged radiative decay.

Overall, the decay analysis confirms that alkali incorporation significantly perturbs the Eu^{3+} local environment. The non-single exponential nature of the decay curves reflects heterogeneous Eu^{3+} environments in LMBO, which are further modulated by the type and concentration of the alkali co-dopant.

3.2.5. *Judd–Ofelt analysis of Eu^{3+} in LMBO*

To further elucidate the radiative processes of Eu^{3+} in LMBO, Judd–Ofelt (J–O) theory was applied (Judd, 1962; Ofelt, 1962). This formalism connects the intensities of the electric-dipole (ED) transitions with three phenomenological parameters, Ω_2, Ω_4, and Ω_6, which provide information about the asymmetry, covalency, and rigidity of the Eu–O coordination environment (Blasse and Grabmaier, 1994; Reisfeld, 1973).

The spontaneous emission probability for an electric–dipole transition $^5D_0 \rightarrow {}^7F\_J$ is given by:

$$A_{0J} = \frac{64\pi^3 e^2 \nu^3}{3h(2J+1)} \cdot \frac{n(n^2+2)^2}{9} \cdot \Omega_\lambda \langle 5D_0 || U^{(\lambda)} || 7F_J \rangle \quad (6)$$

where n is the refractive index of the host, ν is the transition frequency, and $\langle 5D_0 || U^{(\lambda)} || 7F_J \rangle$ are the doubly reduced matrix elements (Carnall et al., 1968). In the present calculations, a refractive index of 1.67 was adopted, which is in good agreement with reported values for borate hosts. The $^5D_0 \rightarrow {}^7F_1$ magnetic-dipole transition, which is insensitive to Ω parameters, was used as an internal reference.

The total radiative probability is obtained by summing over all transitions:

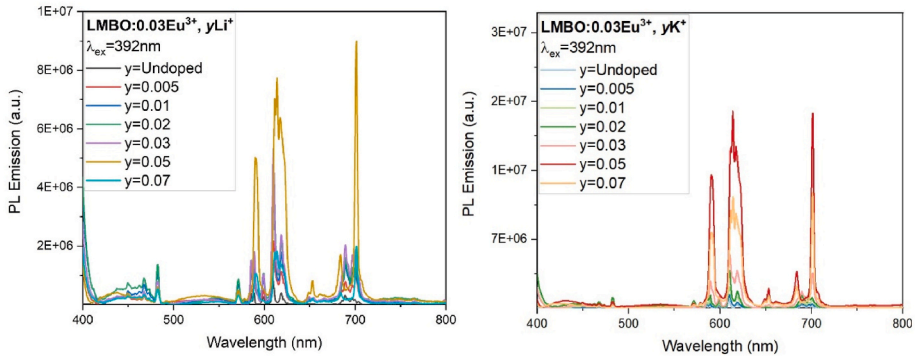

Fig. 7. (a) Photoluminescence emission spectra of LMBO:0.03Eu^{3+}, yLi^{+} (y = 0–0.07) under 392 nm excitation, showing a modest enhancement with maximum intensity at y = 0.05. (b) Corresponding spectra of LMBO:0.03Eu^{3+}, yK^{+}, where co-doping produces a much stronger effect, with the overall PL intensity rising by nearly an order of magnitude at y = 0.05.

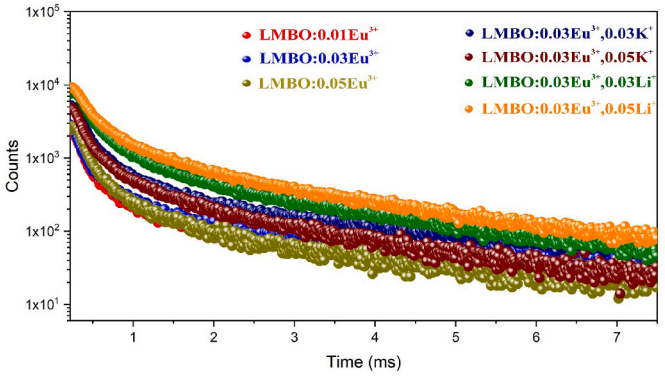

Fig. 8. Decay curves of Eu^{3+} $^5D_0$ emission in LMBO with different Eu^{3+} concentrations and selected Li^{+}/K^{+} co-doped samples under 392 nm excitation, monitored at ~612 nm.

Table 4
Fitted decay parameters (τ_1, τ_2, τ_3 in ms), relative contributions, average lifetime (τ_{avg}), and fit quality (χ^2) for LMBO:Eu^{3+} with and without alkali co-doping.

		Time(ms)	Rel.%	τ_{avg}(ms)	χ^2
LMBO:0.01Eu^{3+}	τ_1	0.0115	45.82	0.827	1.373
	τ_2	0.896	54.18		
LMBO:0.03Eu^{3+}	τ_1	0.0105	34.25	1.382	1.214
	τ_2	0.436	30.33		
	τ_3	2.325	35.42		
LMBO: 0.05Eu^{3+}	τ_1	0.0107	37.25	1.313	1.361
	τ_2	0.453	29.00		
	τ_3	2.196	33.75		
LMBO:0.03Eu^{3+},0.03K^{+}	τ_1	0.0141	48.64	0.937	1.624
	τ_2	1.025	51.36		
LMBO:0.03Eu^{3+},0.05K^{+}	τ_1	0.0110	32.34	1.135	1.179
	τ_2	0.423	27.71		
	τ_3	1.720	39.95		
LMBO:0.03Eu^{3+},0.03Li^{+}	τ_1	0.0085	29.19	0.875	1.864
	τ_2	0.798	40.26		
	τ_2	1.185	30.55		
LMBO:0.03Eu^{3+},0.05Li^{+}	τ_1	0.0144	24.19	1.358	1.240
	τ_2	0.487	28.02		
	τ_3	1.938	47.79		

$$A_{rad} = \sum_J A_{OJ} \tag{7}$$

The branching ratio for a specific transition is defined as:

$$\beta_{0J} = \frac{A_{0J}}{A_{rad}} \tag{8}$$

The radiative lifetime is then calculated as:

$$\tau_{rad} = \frac{1}{A_{rad}} \tag{9}$$

Finally, the quantum efficiency (η) can be estimated by comparing the experimental and calculated lifetimes:

$$\eta = \frac{\tau_{exp}}{\tau_{rad}} \tag{10}$$

The derived J–O parameters, radiative transition probabilities, branching ratios, and lifetimes are summarized in Table 5. The results indicate a pronounced decrease of Ω_2 from 5.19 (Eu^{3+} only) to 2.15 (K^{+}) and 2.22 (Li^{+}), reflecting a reduction in local asymmetry and covalency. Likewise, Ω_4 decreases from 5.74 to 3.21 (K^{+}) and 3.92 (Li^{+}), while Ω_6 becomes nearly negligible (≤0.3). These variations imply that alkali incorporation leads to a more symmetric and less distorted Eu–O coordination environment. It is also worth noting that the Ω_2/Ω_4 ratio decreases from ~0.90 (Eu^{3+}) to ~0.67 (K^{+}) and ~0.57 (Li^{+}), highlighting a stronger suppression of hypersensitive asymmetry relative to lattice rigidity. Such changes provide an additional fingerprint of alkali-induced structural relaxation.

The branching ratios extracted from J–O analysis are in good agreement with experimental emission spectra. For LMBO:0.03Eu^{3+}, β_{02} = 55.9 % and β_{04} = 29.5 %. Upon alkali co-doping, β_{02} decreases to 50.4 % (K^{+}) and 49.4 % (Li^{+}), while β_{04} increases to 30.3 % (K^{+}) and 34.2 % (Li^{+}). This trend is consistent with the observed spectral redistribution: the hypersensitive $^5D_0 \rightarrow {}^7F_2$ band weakens, while the far-red $^5D_0 \rightarrow {}^7F_4$ transition gains relative intensity.

Radiative lifetimes derived from J–O analysis (2.30 ms for Eu^{3+}, 4.21 ms for K^{+} and 3.90 ms for Li^{+})are longer than experimental values, indicating the presence of additional non-radiative channels introduced by lattice distortions. At first sight, this might seem inconsistent with the enhanced far-red emission observed in absolute PL spectra. This apparent inconsistency can be reconciled by noting that Judd–Ofelt parameters represent average local symmetry over all Eu^{3+} sites, whereas the $^5D_0 \rightarrow {}^7F_4$ transition intensity is strongly affected by specific local environments and crystal-field interactions. Alkali co-doping induces charge-compensation effects and strain relaxation, which can redistribute Eu^{3+} ions into energetically favorable sites. These sites may exhibit reduced average asymmetry (lower Ω_2 and Ω_4), yet provide

Table 5
Judd–Ofelt intensity parameters (Ω_2, Ω_4, Ω_6, in 10^{-20} cm^2), radiative transition probabilities (A_{rad}), branching ratios (β, exp. %), radiative lifetimes (τ_{rad}, ms), and quantum efficiencies (η) of Eu^{3+} in LMBO with and without alkali co-doping.

Sample	Ω_2	Ω_4	Ω_6	β_{02}	β_{04}	τ_{rad}	τ_{exp}
LMBO:0.03Eu^{3+}	5.19	5.74	2.70	55.9	29.5	2.30	1.38
LMBO:0.03Eu^{3+},0.05K^+	2.15	3.21	0.29	50.4	30.3	4.21	1.13
LMBO:0.03Eu^{3+},0.05Li^+	2.22	3.92	0.27	49.4	34.2	3.90	0.87

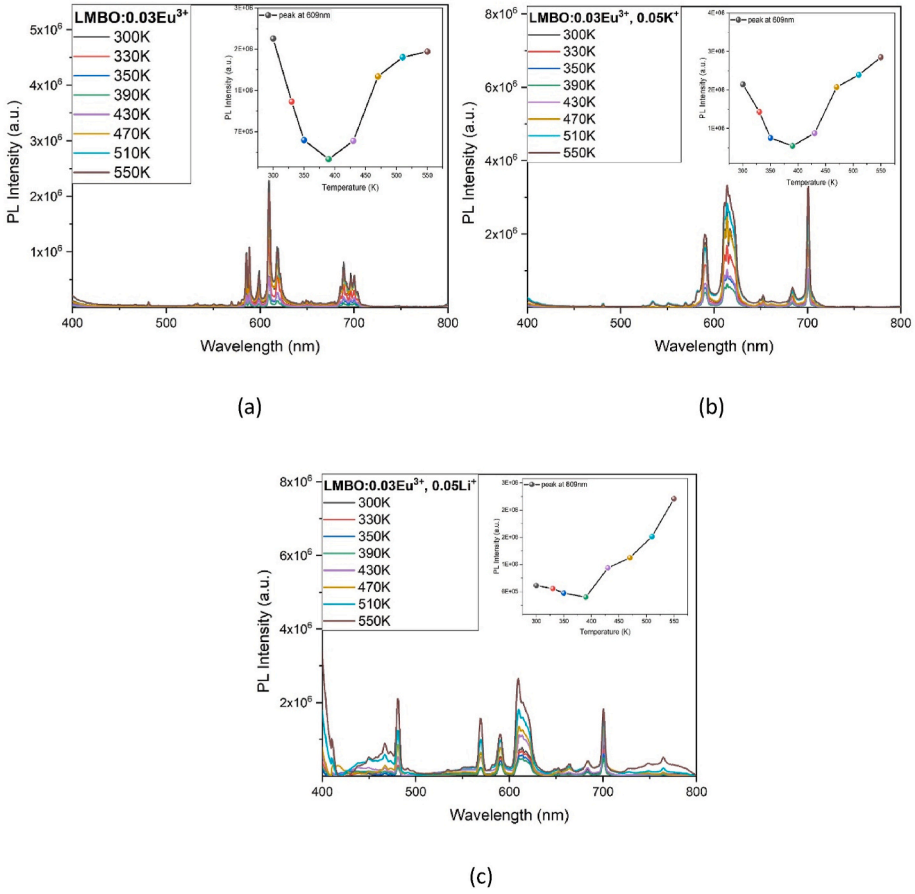

Fig. 9. Temperature-dependent PL emission spectra of LMBO:0.03Eu^{3+} and alkali co-doped samples under 392 nm excitation: (a) LMBO:0.03Eu^{3+}, (b) LMBO:0.03Eu^{3+},0.05K^+, and (c) LMBO:0.03Eu^{3+},0.05Li^+. The inset plots show the integrated intensity of the 609 nm emission as a function of temperature, highlighting distinct quenching and anti-thermal quenching (ATQ) behaviors.

enhanced crystal-field coupling along particular axes, thereby selectively strengthening the $^5D_0 \rightarrow {}^7F_4$ transition. Thus, the far-red enhancement is driven not solely by Ω-parameter magnitudes but also by local site distortions and field-induced transition probabilities.

The requirement of a three-exponential fit for the decay curves further supports the presence of heterogeneous Eu^{3+} environments and/or energy transfer pathways. The shortest lifetime component can be attributed to Eu^{3+} ions located near defects or charge-compensating alkali ions, which favor non-radiative relaxation. The intermediate component likely corresponds to Eu^{3+} in moderately perturbed lattice sites, while the longest lifetime represents Eu^{3+} in more symmetric sites with predominantly radiative decay. The variation of these components with alkali co-doping confirms that Li^+ and K^+ differently perturb the Eu–O coordination. While low-temperature or spectrally resolved lifetime measurements would be required for unambiguous assignments, the present results are consistent with site heterogeneity and redistribution of Eu^{3+} emission pathways. However, it should be emphasized that J–O parameters are derived from relative line strengths and therefore reflect redistribution among transitions rather than the total photon yield. The anomalous reinforcement of the $^5D_0 \rightarrow {}^7F_4$ transition in LMBO:Eu^{3+},K^+ is thus not caused by an increase of Ω_4, but arises from oscillator strength redistribution, local-field effects, and modified excitation–emission pathways. Similar phenomena have been observed in Eu^{3+} systems where non-centrosymmetric site occupation leads to narrow-band red emission with high color purity (Dang et al., 2021; Souadi et al., 2023). Overall, the J–O analysis demonstrates that alkali co-doping substantially modifies the Eu^{3+} site environment in LMBO. K^+ doping, in particular, suppresses the hypersensitive $^5D_0 \rightarrow {}^7F_2$ band while enhancing the far-red $^5D_0 \rightarrow {}^7F_4$ emission, despite lowering Ω_2, Ω_4, and η. This distinctive combination of high absolute far-red intensity with tunable spectral weight underscores the promise of LMBO:Eu^{3+},K^+ as a far-red phosphor for pc-wLEDs and plant growth applications.

3.2.6. *Thermal stability and activation energy analysis*

The thermal evolution of the PL emission spectra of LMBO:Eu^{3+} and its alkali co-doped derivatives is shown in Fig. 9. All spectra are dominated by the characteristic Eu^{3+} $^5D_0 \rightarrow {}^7F_J$ transitions, yet their relative intensities strongly depend on temperature and the presence of alkali ions. The 609 nm $^5D_0 \rightarrow {}^7F_2$ band was chosen as a probe for quantitative analysis, and its integrated intensity was monitored between 300 and

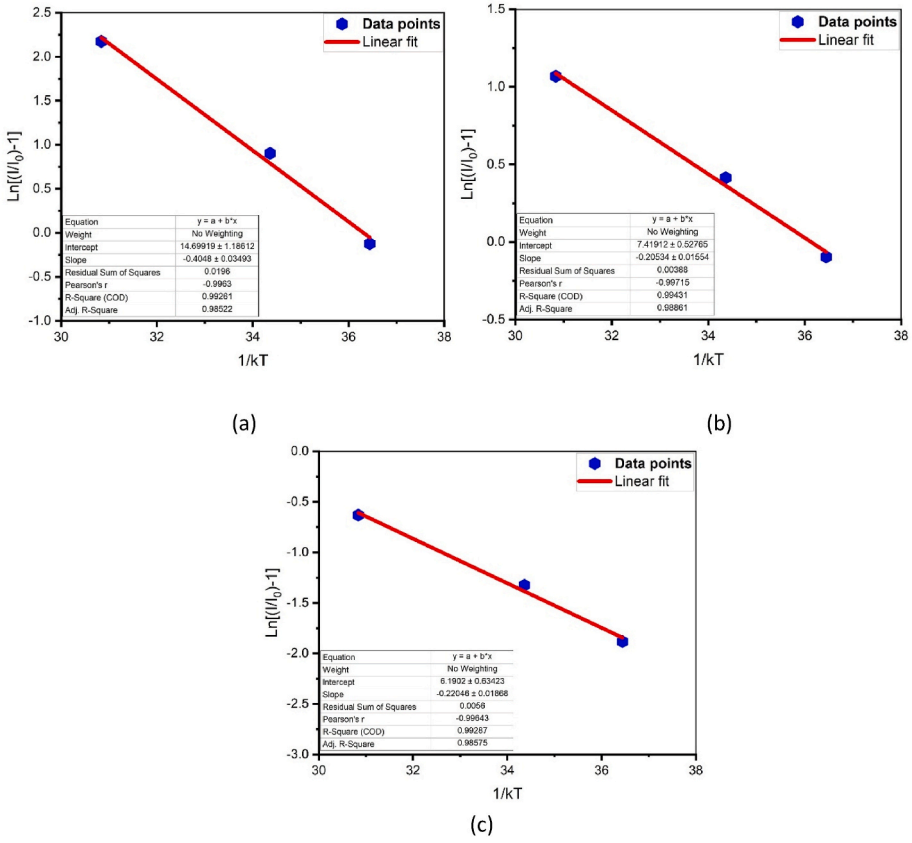

Fig. 10. Arrhenius plots of the 609 nm emission for LMBO:Eu^{3+} and alkali co-doped samples: (a) Eu^{3+} (E_a = 0.404 eV), (b) Eu^{3+},0.05K^+ (E_a = 0.205 eV, moderate ATQ above 470 K), and (c) Eu^{3+},0.05Li^+ (E_a = 0.220 eV, strong ATQ up to 550 K).

550 K.

In the undoped LMBO:0.03Eu^{3+} sample (Fig. 9a), the emission intensity decreases rapidly up to ~390 K, indicating conventional thermal quenching (TQ). A partial recovery occurs above 430 K, suggesting that thermally assisted repopulation compensates part of the non-radiative loss. By comparison, K^+ co-doping (Fig. 9b) leads to a weaker quenching regime up to ~390 K, followed by moderate anti-thermal quenching (ATQ) above 470 K, where the emission exceeds the room-temperature value. The most pronounced effect is observed for Li^+ (Fig. 9c), where the emission intensity increases almost monotonically with temperature, reaching nearly four times its 300 K value at 550 K. This robust ATQ demonstrates the strong influence of alkali co-doping on high-temperature stability.

To evaluate the thermal activation energies of the non-radiative channels, the integrated PL intensities were analyzed using the Arrhenius relation (Blasse and Grabmaier, 1994):

$$I(T) = \frac{I_0}{1 + Cexp\left(-\frac{E_a}{k_B T}\right)} \tag{11}$$

where I(T) is the emission intensity at temperature T, I_0 is the initial intensity at 300 K, C is a fitting constant, k_B is Boltzmann's constant, and E_a is the activation energy for non-radiative processes. Linearization gives

$$ln\left(\frac{I_0}{I(T)} - 1\right) = lnC - \frac{E_a}{k_B}\frac{1}{T} \tag{12}$$

Thus, a plot of $ln[(I_0/I) - 1]$ versus $1/T$ yields a straight line in the quenching-dominated region, with slope equal to $-E_a/k_B$. The corresponding Arrhenius plots are shown in Fig. 10a–c.

From linear fits, the activation energies were extracted as 0.404 eV for LMBO:0.03Eu^{3+}, 0.205 eV for LMBO:0.03Eu^{3+},0.05K^+, and 0.220 eV for LMBO:0.03Eu^{3+},0.05Li^+. The higher barrier in the undoped host explains its conventional quenching, while alkali incorporation lowers this barrier and simultaneously enables thermally assisted processes. K^+ facilitates moderate ATQ above 470 K, whereas Li^+ creates shallow traps that yield strong ATQ with nearly fourfold intensity reinforcement at 550 K.

At first glance, a lower activation energy is usually associated with stronger quenching rather than ATQ. In the present case, however, the reduced barrier does not solely promote non-radiative relaxation but also facilitates thermally assisted feeding into Eu^{3+} excited states, either from shallow trap levels or through host-to-Eu^{3+}/CTB transfer channels introduced by alkali co-doping. Consequently, the lower E_a values observed here reflect a balance between enhanced non-radiative access and the simultaneous activation of radiative feeding pathways, which ultimately leads to anti-thermal quenching rather than conventional quenching.

These results confirm that alkali co-doping not only modifies the local Eu^{3+} environment at room temperature but also redefines the balance between radiative and non-radiative channels at elevated temperatures. The coexistence of lower activation barriers with enhanced ATQ highlights the synergy between lattice distortion, phonon coupling, and thermally assisted population feeding. Comparable behaviors have been reported in other Eu^{3+}-activated oxide hosts (Dang et al., 2021; Souadi et al., 2023).

In the present LMBO system, no evidence of negative thermal expansion was detected in the XRD analysis, making this mechanism unlikely. Instead, the presence of BO_4^{3-} groups suggests that thermally assisted host-to-Eu^{3+} energy transfer may be the dominant contributor, while alkali co-doping modifies the Eu–O coordination and the CTB energy level, enabling additional feeding into Eu^{3+} excited states. Therefore, the ATQ behavior observed in LMBO:Eu^{3+},M^+ phosphors is

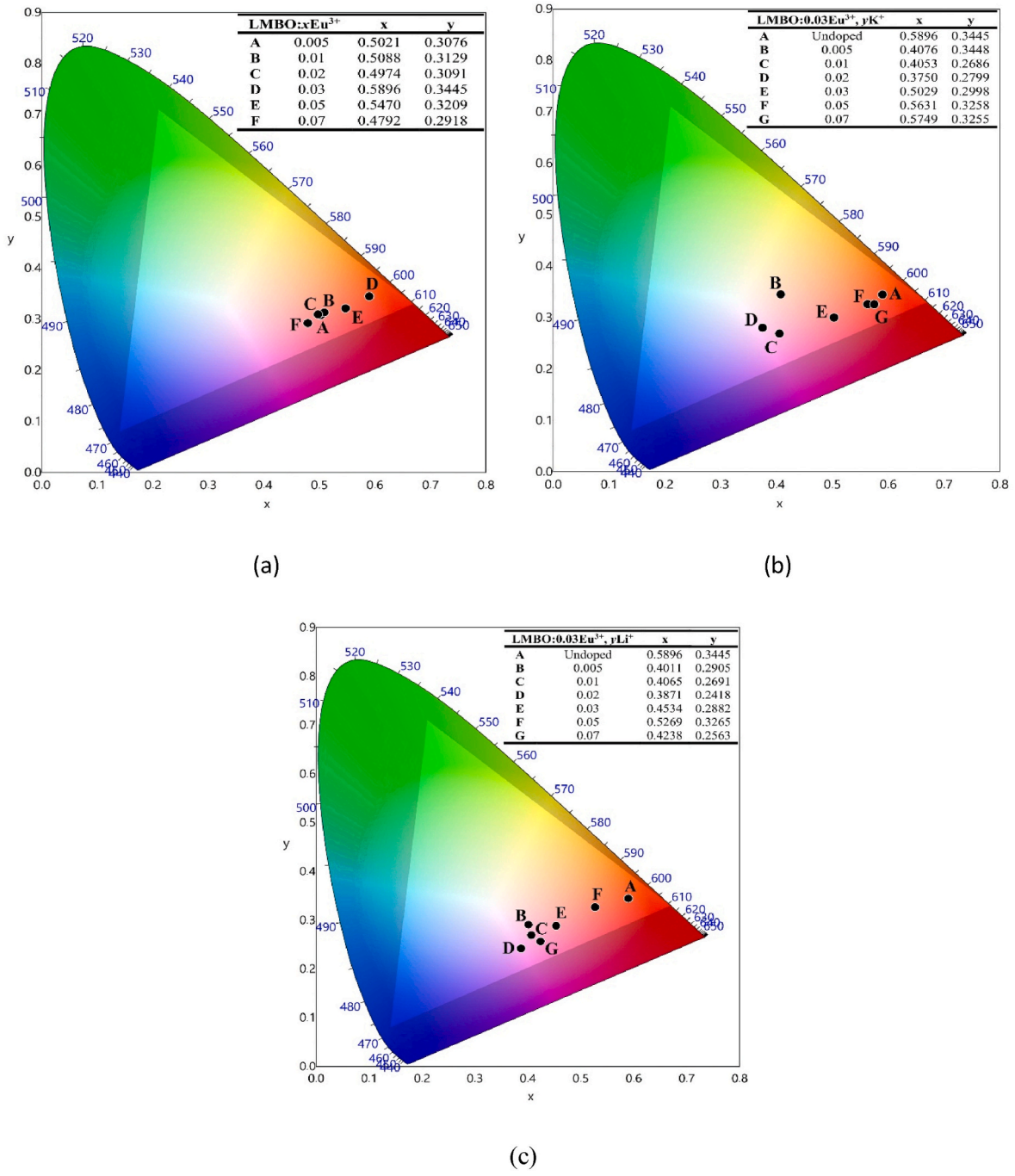

Fig. 11. CIE chromaticity diagrams of LMBO phosphors: (a) LMBO:xEu^{3+} with varying Eu^{3+} concentrations, (b) LMBO:0.03Eu^{3+},yK^{+} with different K^{+} co-doping levels, and (c) LMBO:0.03Eu^{3+},yLi^{+} with different Li^{+} co-doping levels.

most consistently explained by a combination of host-to-Eu^{3+} transfer and CTB-related processes rather than by lattice contraction effects.

3.2.7. CIE chromaticity coordinates and correlated color temperature (CCT) analysis

The CIE chromaticity diagrams of LMBO:xEu^{3+}, LMBO:0.03Eu^{3+}, yK^{+}, and LMBO:0.03Eu^{3+},yLi^{+} phosphors are presented in Fig. 11a–c. All emission points are located in the reddish region, consistent with the characteristic $^5D_0 \rightarrow {}^7F_2$ transition of Eu^{3+}. Minor shifts in the co-ordinates are observed with increasing Eu^{3+} concentration and alkali co-doping, reflecting subtle modifications in the Eu–O local environment.

The corresponding correlated color temperature (CCT) values confirm this reddish character. For Eu^{3+} single-doped LMBO, CCT values remain in the warm range, between ~1627 K (x = 0.02) and ~1815 K (x = 0.03). K^{+} co-doping extends the variation, giving values from ~1702 K up to ~3091 K: low K^{+} contents result in slightly cooler tones, whereas higher contents reduce the CCT below 2000 K, reinforcing red emission. In contrast, Li^{+} co-doping maintains lower CCT values between ~1621 and 2420 K, consistently favoring warm-red emission.

The CCT values were calculated from the CIE chromaticity co-ordinates using McCamy's empirical formula (McCamy, 1992):

$$CCT = -449n^3 + 3525n^2 - 6823.3n + 5520.33, \text{ where } n = (x - 0.3320)/(y - 0.1858)$$

These results demonstrate that while Eu^{3+} doping alone ensures strong reddish emission, alkali co-doping allows further modulation. Li^{+}

incorporation stabilizes the red component, whereas K^+ provides wider tunability from moderately cool to warm-red regions, making LMBO:Eu^{3+} phosphors versatile candidates for solid-state lighting applications.

To contextualize the luminescence performance of the LMBO:Eu^{3+},M^+ phosphors, it is instructive to compare them with the widely used benchmark Y_2O_3:Eu^{3+} phosphor. Y_2O_3:Eu^{3+} is recognized for its strong red emission ($^5D_0 \rightarrow {}^7F_2$ at ~609–612 nm) and high color purity, which makes it one of the most common red phosphors for display and lighting applications (Dutta et al., 2025; Muresan et al., 2009). However, despite its excellent room-temperature brightness, Y_2O_3:Eu^{3+} typically suffers from thermal quenching above ~420–450 K, leading to a rapid decrease in emission intensity. In contrast, the LMBO:Eu^{3+},M^+ system reported here demonstrates unusual anti-thermal quenching behavior: Li^+ co-doping enhances the emission intensity nearly fourfold at 550 K, while K^+ co-doping stabilizes the emission above 470 K. Such high-temperature stability provides a distinct advantage over conventional Y_2O_3:Eu^{3+}, which generally requires additional structural modifications (e.g., surface coating or composite hosts) to mitigate thermal degradation. Thus, while the room-temperature emission intensity of LMBO:Eu^{3+} is comparable to that of Y_2O_3:Eu^{3+}, its superior thermal stability positions it as a promising red phosphor for high-power pc-WLEDs and plant-growth lighting where devices operate at elevated temperatures.

In addition, several recent studies have also reported Eu^{3+} anti-thermal quenching and alkali co-doping effects in different hosts. For instance, Eu^{3+},Li^+ co-doped $SmCa_4O(BO_3)_3$ exhibited negative thermal quenching and enhanced emission stability (Altowyan et al., 2025b). Eu^{3+} single-doped phosphors with multicolor-tunable ATQ behavior have also been reported (Shi et al., 2023), while a novel Eu^{3+}-activated red phosphor based on $In_{0.5}Sc_{1.5}(MoO_4)_3$ showed anti-thermal quenching due to negative thermal expansion (Tian et al., 2024). These reports emphasize that alkali co-doping and host lattice dynamics are critical factors for stabilizing Eu^{3+} luminescence at elevated temperatures, which strongly supports the unusual ATQ behavior observed in LMBO:Eu^{3+},M^+ phosphors.

4. Conclusions

Eu^{3+}-activated LMBO phosphors co-doped with alkali ions show remarkable modifications in both emission intensity and thermal stability. Structural analyses demonstrated that Li^+ and K^+ incorporation perturbs the Eu–O coordination environment, leading to redistribution of oscillator strength among the $^5D_0 \rightarrow {}^7F_J$ transitions. Photoluminescence studies revealed that K^+ co-doping strongly enhances the far-red $^5D_0 \rightarrow {}^7F_4$ emission, while Li^+ produces a more moderate redistribution effect. Judd–Ofelt analysis confirmed that alkali-induced symmetry changes influence radiative parameters and quantum efficiencies, highlighting the sensitivity of Eu^{3+} emission to local lattice distortions.

Temperature-dependent PL measurements further established a clear difference in high-temperature behavior: undoped LMBO:Eu^{3+} exhibited conventional quenching with an activation barrier of 0.404 eV, K^+ reduced the barrier to 0.205 eV and induced moderate anti-thermal quenching, while Li^+ produced strong anti-thermal quenching, yielding nearly a fourfold intensity increase at 550 K. These results demonstrate that alkali co-doping simultaneously lowers the quenching barrier and enables thermally assisted population feeding, ultimately stabilizing or enhancing Eu^{3+} emission at elevated temperatures.

Such dual functionality establishes LMBO:Eu^{3+},M^+ phosphors as promising candidates for high-power pc-wLEDs, plant-growth illumination, and other optoelectronic applications requiring robust performance under thermal stress.

CRediT authorship contribution statement

V. Onar: Methodology, Investigation, Funding acquisition. **E. Ekdal Karali:** Software, Methodology, Investigation. **Abeer S. Altowyan:** Writing – original draft, Methodology, Investigation, Funding acquisition. **H. Aydin:** Software, Methodology, Investigation. **U.H. Kaynar:** Software, Methodology, Investigation, Funding acquisition. **C. Gök:** Investigation, Data curation, Conceptualization. **M.B. Coban:** Methodology, Investigation, Formal analysis, Data curation. **Jabir Hakami:** Investigation, Data curation, Conceptualization. **Y. Ozcan:** Software, Resources, Methodology. **A. Canimoglu:** Methodology, Investigation, Conceptualization. **N. Can:** Writing – review & editing, Writing – original draft.

Declaration of competing interest

The authors declare that they have no known competing financial interests or personal relationships that could have appeared to influence the work reported in this paper.

Acknowledgment

The authors gratefully acknowledge the financial support provided by Pamukkale University under BAP Project No. 2025. HZDP-001. This study was supported by the Princess Nourah bint Abdulrahman University Researchers Supporting Project (PNURSP2025R16), Princess Nourah bint Abdulrahman University, Riyadh, Saudi Arabia. Additional support was provided by the Scientific and Technological Research Council of Turkey (TÜBİTAK) through the project numbered 223M036 under the TUBITAK-1001 program, as well as through the 2221 Fellowship Program for Visiting Scientists and Scientists on Sabbatical Leave. The authors gratefully acknowledge these institutions for their valuable contributions.

Data availability

Data will be made available on request.

References

Altowyan, A.S., Kaynar, U.H., Aydin, H., Coban, M.B., Portakal, Z.G., Akça-Özalp, S., Hakami, J., Ayvacikli, M., Topaksu, M., Can, N., 2025a. Enhanced photoluminescence properties of Eu^{3+}/Li^+ co-doped ZrO_2: a focus on red and far-red emissions. J. Photochem. Photobiol. Chem. 466, 116408. https://doi.org/10.1016/j.jphotochem.2025.116408.

Altowyan, A.S., Kaynar, U.H., Çin, E.A., Karaman, T., Aydin, H., Coban, M.B., Hakami, J., Can, N., 2025b. Eu^{3+} and Li^+ Co-doped $SmCa_4O(BO_3)_3$ phosphors: negative thermal quenching and photoluminescence properties. J. Alloys Compd. 1021, 179766. https://doi.org/10.1016/j.jallcom.2025.179766.

Altowyan, A.S., Kaynar, U.H., Hakami, J., Coban, M.B., Ayvacikli, M., Aydin, H., Canimoglu, A., Can, N., 2024. Integrating K^+ into Eu and Tb doped $GdCa_4O(BO_3)_3$: a dual study on photoluminescence and structure. Sensors Actuators A Phys 373, 115453. https://doi.org/10.1016/j.sna.2024.115453.

Balachander, L., Ramadevudu, G., Shareefuddin, M., Sayanna, R., Venudhar, Y.C., 2013. IR analysis of borate glasses containing three alkali oxides. Sci. Asia 39, 278. https://doi.org/10.2306/scienceasia1513-1874.2013.39.278.

Blasse, G., 1968. Energy transfer in oxidic phosphors. Phys. Lett. 28, 444–445. https://doi.org/10.1016/0375-9601(68)90486-6.

Blasse, G., Grabmaier, B.C., 1994. Luminescent Materials. Springer Berlin Heidelberg, Berlin, Heidelberg. https://doi.org/10.1007/978-3-642-79017-1.

Boda, R., Shareefuddin, M.D., Chary, M.N., Sayanna, R., 2016. FTIR and optical properties of europium doped lithium zinc bismuth borate glasses. Mater. Today Proc. 3, 1914–1922. https://doi.org/10.1016/j.matpr.2016.04.092.

Carnall, W.T., Fields, P.R., Rajnak, K., 1968. Electronic energy levels in the trivalent lanthanide aquo ions. I. Pr^{3+}, Nd^{3+}, Pm^{3+}, Sm^{3+}, Dy^{3+}, Ho^{3+}, Er^{3+}, and Tm^{3+}. J. Chem. Phys. 49, 4424–4442. https://doi.org/10.1063/1.1669893.

Chi, F., Wei, X., Zhou, S., Chen, Y., Duan, C., Yin, M., 2018. Enhanced $^5D_0 \rightarrow {}^7F_4$ transition and optical thermometry of garnet type $Ca_3Ga_2Ge_3O_{12}$:Eu^{3+} phosphors. Inorg. Chem. Front. 5, 1288–1293. https://doi.org/10.1039/C8QI00199E.

Dang, P., Li, G., Yun, X., Zhang, Q., Liu, D., Lian, H., Shang, M., Lin, J., 2021. Thermally stable and highly efficient red-emitting Eu^{3+}-doped $Cs_3GdGe_3O_9$ phosphors for WLEDs: non-concentration quenching and negative thermal expansion. Light Sci. Appl. 10, 29. https://doi.org/10.1038/s41377-021-00469-x.

Dexter, D.L., 1953. A theory of sensitized luminescence in solids. J. Chem. Phys. 21, 836–850. https://doi.org/10.1063/1.1699044.

Diputra, A.H., Hariscandra Dinatha, I.K., Yusuf, Y., 2025. A comparative X-ray diffraction analysis of Sr^{2+} substituted hydroxyapatite from sand lobster shell waste

using various methods. Heliyon 11, e41781. https://doi.org/10.1016/j.heliyon.2025.e41781.

Dubey, V., Kaur, J., Agrawal, S., Suryanarayana, N.S., Murthy, K.V.R., 2014. Effect of Eu^{3+} concentration on photoluminescence and thermoluminescence behavior of YBO_3:Eu^{3+} phosphor. Superlattice. Microst. 67, 156–171. https://doi.org/10.1016/j.spmi.2013.12.026.

Dutta, M., Kalita, J.M., Wary, G., 2025. Green to orange colour tuneable Y_2O_3:Eu^{3+} phosphor: a study of structural, compositional and optical properties. Ceram. Int. 51, 23354–23366. https://doi.org/10.1016/j.ceramint.2025.03.024.

El Jouhari, N., Parent, C., Le Flem, G., 1996. Photoluminescence of Ce^{3+}, Tb^{3+}, and Mn^{2+} in glasses of base composition $LaMgB_5O_{10}$. J. Solid State Chem. 123, 398–407. https://doi.org/10.1006/jssc.1996.0195.

Fouassier, C., Saubat, B., Hagenmuller, P., 1981. Self-quenching of Eu^{3+} and Tb^{3+} luminescence in $LaMgB_5O_{10}$: a host structure allowing essentially one-dimensional interactions. J. Lumin. 23, 405–412. https://doi.org/10.1016/0022-2313(81)90143-5.

Gaikwad, A., Parauha, Y.R., Dabre, K.V., Dhoble, S.J., 2025. Synthesis and luminescence properties of $Na_3SrB_5O_{10}$:Eu^{3+} glass samples for solid-state lighting application. Chem. Phys. Impact 10, 100815. https://doi.org/10.1016/j.chphi.2025.100815.

George, A., Sreeja, E., Jose, A., Vidhu, V.K., Francis, T., Biju, P.R., 2025. Photoluminescence characteristics and Judd–Ofelt analysis of Eu^{3+} doped $Ca_3Nb_2O_8$ phosphor for photonic devices and red laser applications. J. Alloys Compd. 1010, 178177. https://doi.org/10.1016/j.jallcom.2024.178177.

Gharavi-Naeini, J., Yoo, K.W., Stump, N.A., 2018. Characterization of barium borate frameworks using Raman spectroscopy. Appl. Spectrosc. 72, 627–633. https://doi.org/10.1177/0003702817748952.

Hakami, J., Kaynar, U.H., Coban, M.B., Aydin, H., Alamri, R., Jabali, D.A., Can, N., 2025. Optical performance and luminescence properties of Dy^{3+}-doped $LaMgB_5O_{10}$ phosphors. Inorg. Chem. Commun. 171, 113540. https://doi.org/10.1016/j.inoche.2024.113540.

Hepp, A., Baerlocher, C., 1988. Learned peak shape functions for powder diffraction data. Aust. J. Phys. 41, 229. https://doi.org/10.1071/PH880229.

Hölsä, J., Leskelä, M., 1985. Fluorescence spectrum, energy level scheme and crystal field analysis of europium(+III) doped lanthanum magnesium borate $LaMgB_5O_{10}$:Eu^{3+}. Mol. Phys. 54, 657–667. https://doi.org/10.1080/00268978500100511.

Hong, J.H., Lee, J.Y., Kang, J.H., Lee, J.Y., Jang, H.S., Cho, S.-Y., Kim, D.H., 2022. Microstructure and photoluminescence of Eu-doped $Sr_3Al_2O_6$ phosphors calcined with and without H_3BO_3 flux. Ceram. Int. 48, 32886–32893. https://doi.org/10.1016/j.ceramint.2022.07.216.

Jabali, D.A., Madkhli, A.Y., Souadi, G., Kaynar, Ü.H., Coban, M.B., Madkhali, O., Ayvacikli, M., Amri, N., Can, N., 2024. Temperature-responsive insights: investigating Eu^{3+} and Dy^{3+} activated yttrium calcium oxyborate phosphors for structure and luminescence. Appl. Radiat. Isot. 206, 111214. https://doi.org/10.1016/j.apradiso.2024.111214.

Jambhale, M.P., Palan, C.B., Hargunani, S.P., 2025. A comprehensive review on rare earth activated borate phosphors: synthesis, properties, and applications. Int. J. Sci. Res. Sci. Technol. 12, 204–208.

Jayakiruba, S., Chandrasekaran, S.S., Murugan, P., Lakshminarasimhan, N., 2017. Excitation-dependent local symmetry reversal in single host lattice $Ba_2A(BO_3)_2$:Eu^{3+} [A = Mg and Ca] phosphors with tunable emission colours. Phys. Chem. Chem. Phys. 19, 17383–17395. https://doi.org/10.1039/C7CP02740K.

Judd, B.R., 1962. Optical absorption intensities of rare-earth ions. Phys. Rev. 127, 750–761. https://doi.org/10.1103/PhysRev.127.750.

Jüstel, T., Nikol, H., Ronda, C., 1998. New developments in the field of luminescent materials for lighting and displays. Angew. Chem. Int. Ed. 37, 3084–3103. https://doi.org/10.1002/(SICI)1521-3773(19981204)37:22<3084::AID-ANIE3084>3.0.CO;2-W.

K, N.R., Vidya, Y.S., Manjunatha, H.C., Ramaraghavulu, R., Munirathnam, R., Manjunatha, S.B.V.P., Shivanna, M.H.B., 2025. Role of Eu^{3+} concentration on photoluminescence and electrochemical studies of $Bi_2Cr_4O_{15}$ nanoparticles. Mater. Sci. Eng. B 322, 118540. https://doi.org/10.1016/j.mseb.2025.118540.

Kaynar, U.H., Coban, M.B., Hakami, J., Altowyan, A.S., Aydin, H., Ayvacikli, M., Can, N., 2024. Enhanced luminescence of Eu^{3+} in $LaAl_2B_4O_{10}$ via energy transfer from Dy^{3+} doping. Spectrochim. Acta Part A Mol. Biomol. Spectrosc. 321, 124711. https://doi.org/10.1016/j.saa.2024.124711.

Lin, C.K., Yu, M., Pang, M.L., Lin, J., 2006. Photoluminescent properties of sol–gel derived (La,Gd)MgB_5O_{10}:Ce^{3+}/Tb^{3+} nanocrystalline thin films. Opt. Mater. 28, 913–918. https://doi.org/10.1016/j.optmat.2005.04.009.

Ling-Hu, P., Guo, X., Hu, J., Deng, C., Cui, R., 2024. Anomalous $^5D_0 \rightarrow {}^7F_4$ transition of Eu^{3+}-doped $BaLaGaO_4$ phosphors for WLEDs and plant growth applications. Adv. Opt. Mater. 12. https://doi.org/10.1002/adom.202301760.

Liu, C., Zhou, Z., Zhang, Y., 2019. Synthesis and luminescence properties of novel red-emitting Na_2ZnSiO_4:Eu^{3+} phosphor with intense $^5D_0 \rightarrow {}^7F_4$ transition and high quantum yield. J. Alloys Compd. 787, 1158–1162. https://doi.org/10.1016/j.jallcom.2019.02.140.

Lokeswara Reddy, G.V., Rama Moorthy, L., Packiyaraj, P., Jamalaiah, B.C., 2013. Optical characterization of $YAl_3(BO_3)_4$:Dy^{3+}–Tm^{3+} phosphors under near UV excitation. Opt. Mater. 35, 2138–2145. https://doi.org/10.1016/j.optmat.2013.05.038.

McCamy, C.S., 1992. Correlated color temperature as an explicit function of chromaticity coordinates. Color Res. Appl. 17, 142–144. https://doi.org/10.1002/col.5080170211.

Mitina, D.D., Maltsev, V.V., Deyneko, D.V., Volkova, E.A., Koporulina, E.V., Kuzmin, N. N., Kosorukov, V.L., Jiliaeva, A.I., Naprasnikov, D.A., 2023. Luminescence properties of Tb^{3+}- and Eu^{3+}-doped lanthanum magnesium pentaborates. Inorg. Mater. 59, 1085–1096. https://doi.org/10.1134/S0020168523100096.

Monshi, A., Foroughi, M.R., Monshi, M.R., 2012. Modified scherrer equation to estimate more accurately nano-crystallite size using XRD. World J. Nano Sci. Eng. 2, 154–160. https://doi.org/10.4236/wjnse.2012.23020.

Morebodi, K.B., Ogugua, S.N., Kumar, V., Swart, H.C., 2024. The effects of Eu^{3+} concentration on the photoluminescence of $Na_4Ca(PO_3)_6$ phosphors prepared by a solid-state reaction method. Chem. Phys. Impact 9, 100718. https://doi.org/10.1016/j.chphi.2024.100718.

Muresan, L., Popovici, E.J., Imre-Lucaci, F., Grecu, R., Indrea, E., 2009. Studies on Y_2O_3: Eu phosphor with different particle size prepared by wet chemical method. J. Alloys Compd. 483, 346–349. https://doi.org/10.1016/j.jallcom.2008.08.087.

Ofelt, G.S., 1962. Intensities of crystal spectra of rare-earth ions. J. Chem. Phys. 37, 511–520. https://doi.org/10.1063/1.1701366.

Reisfeld, R., 1973. Spectra and energy transfer of rare earths in inorganic glasses, 53–98. https://doi.org/10.1007/3-540-06125-8_2.

Sakirzanovas, S., Katelnikovas, A., Bettentrup, H., Kareiva, A., Jüstel, T., 2011. Synthesis and photoluminescence properties of Sm^{3+}-doped $LaMgB_5O_{10}$ and $GdMgB_5O_{10}$. J. Lumin. 131, 1525–1529. https://doi.org/10.1016/j.jlumin.2011.02.005.

Saubat, B., Fouassier, C., Hagenmuller, P., Bourcet, J.C., 1981. Luminescent efficiency of Eu^{3+} and Tb^{3+} in $LaMgB_5O_{10}$ — type borates under excitation from 100 to 400 nm. Mater. Res. Bull. 16, 193–198. https://doi.org/10.1016/0025-5408(81)90081-7.

Sekrafi, H.E., Hergli, E., Ferdov, S., Coutinho, P.J.G., Rebouta, L., 2025. Understanding the structural and optical evolution of Eu^{3+} and Dy^{3+} co-doped YVO_4 phosphors across concentration series for lighting applications. J. Alloys Compd. 1010, 177389. https://doi.org/10.1016/j.jallcom.2024.177389.

Shablinskii, A.P., Povolotskiy, A.V., Yuriev, A.A., Biryukov, Y.P., Bubnova, R.S., Avdontceva, M.S., Janson, S.Y., Filatov, S.K., 2023. Novel red-emitting $BaBi_2B_4O_{10}$: Eu^{3+} phosphors: synthesis, crystal structure and luminescence. Symmetry (Basel). 15, 918. https://doi.org/10.3390/sym15040918.

Shannon, R.D., 1976. Revised effective ionic radii and systematic studies of interatomic distances in halides and chalcogenides. Acta Crystallogr., Sect. A 32, 751–767. https://doi.org/10.1107/S0567739476001551.

Shi, X., Xue, Y., Mao, Q., Pei, L., Li, X., Liu, M., Zhang, Q., Zhong, J., 2023. Eu $^{3+}$ single-doped phosphor with antithermal quenching behavior and multicolor-tunable properties for luminescence thermometry. Inorg. Chem. 62, 893–903. https://doi.org/10.1021/acs.inorgchem.2c03699.

Somaily, D.A.E., Altowyan, A.S., Kaynar, U.H., Aydin, H., Hakami, J., Coban, M.B., Zelai, T., Can, N., 2025. Tunable luminescence and structural modifications in Eu^{3+}/Li^+ Co-doped $YBa_3(BO_3)_3$ phosphors for LEDs. Mater. Res. Bull. 189, 113453. https://doi.org/10.1016/j.materresbull.2025.113453.

Souadi, G., Kaynar, Ü.H., Ayvacikli, M., Can, N., 2023. Luminescence of undoped and Eu3+ activated zinc gallate phosphor: synthesis, unusual intense $^5D_0 \rightarrow {}^7F_4$ red emission. Appl. Radiat. Isot. 199, 110905. https://doi.org/10.1016/j.apradiso.2023.110905.

Spelthann, S., Thiem, J., Melchert, O., Komban, R., Gimmler, C., Demicran, A., Ruehl, A., Ristau, D., 2023. Predicting the excitation dynamics in lanthanide nanoparticles. Adv. Opt. Mater. 11. https://doi.org/10.1002/adom.202300096.

Tanner, P.A., Thor, W., Zhang, Y., Wong, K.-L., 2022. Energy transfer mechanism and quantitative modeling of rate from an Antenna to a lanthanide ion. J. Phys. Chem. A 126, 7418–7431. https://doi.org/10.1021/acs.jpca.2c03965.

Tawalare, P.K., 2022. Luminescent inorganic mixed borate phosphors materials for lighting. Luminescence 37, 1226–1245. https://doi.org/10.1002/bio.4301.

Tian, T., Wang, Z., Mao, C., Chen, M., Chu, Y., Li, Y., 2024. Structure, luminescence properties and anti-thermal quenching of a novel Eu^{3+}-activated red phosphor based on the negative thermal expansion material $In_{0.5}Sc_{1.5}(MoO_4)_3$. J. Alloys Compd. 973, 172887. https://doi.org/10.1016/j.jallcom.2023.172887.

Tiwari, A., Dhoble, S.J., 2025. Borate-based luminescent materials: a comprehensive review of structural influences on thermal stability and luminescence characteristics. J. Lumin. 287, 121490. https://doi.org/10.1016/j.jlumin.2025.121490.

Volkova, E.A., Maltsev, V.V., Antipin, A.M., Deyneko, D.V., Nikiforov, I.V., Spassky, D.A., Marchenko, E.I., Mitina, D.D., Kosorukov, V.L., Yapaskurt, V.O., Naprasnikov, D.A., Koporulina, E.V., 2023. The synthesis, structure, and luminescent properties of $TmMgB_5O_{10}$ crystals. Materials 16, 6084. https://doi.org/10.3390/ma16186084.

Williamson, G., Hall, W., 1953. X-ray line broadening from filed aluminium and wolfram. Acta Metall. 1, 22–31. https://doi.org/10.1016/0001-6160(53)90006-6.

Xiang, Y., Zheng, Y., Yang, L., Li, M., Mao, Y., Zhu, J., 2022. Exploring a new Dy^{3+}-activated borotellurate phosphor with thermally stable photoluminescence. J. Alloys Compd. 919, 165837. https://doi.org/10.1016/j.jallcom.2022.165837.